Atmospheric Research 264 (2021) 105858

Contents lists available at ScienceDirect

Atmospheric Research

journal homepage: www.elsevier.com/locate/atmosres

A rapid refresh ensemble based data assimilation and forecast system for the RELAMPAGO field campaign

María Eugenia Dillon [a,b,*], Paula Maldonado [b,c], Paola Corrales [a,c,d], Yanina García Skabar [a,b,e], Juan Ruiz [a,c,d,e], Maximiliano Sacco [b], Federico Cutraro [b], Leonardo Mingari [f], Cynthia Matsudo [b], Luciano Vidal [b], Martin Rugna [b], María Paula Hobouchian [b], Paola Salio [a,c,d,e], Stephen Nesbitt [g], Celeste Saulo [a,b], Eugenia Kalnay [h], Takemasa Miyoshi [i]

[a] CONICET (Consejo Nacional de Investigaciones Científicas y Técnicas), Argentina
[b] Servicio Meteorológico Nacional de, Argentina
[c] Departamento de Ciencias de la Atmósfera y los Océanos, Facultad de Ciencias Exactas y Naturales, Universidad de Buenos Aires, Argentina
[d] Centro de Investigaciones del Mar y la Atmósfera (CONICET-UBA), Argentina
[e] Instituto Franco-Argentino sobre Estudios de Clima y sus Impactos (UMI-3351 IFAECI/CNRS-CONICET-UBA), Argentina
[f] Barcelona Supercomputing Center, Spain
[g] Department of Atmospheric Sciences, University of Illinois at Urbana-Champaign, USA
[h] Department of Atmospheric and Oceanic Sciences, University of Maryland, USA
[i] RIKEN Center for Computational Science, Japan

ARTICLE INFO

Keywords:
Regional data assimilation
Regional ensemble forecasts
RELAMPAGO

ABSTRACT

This paper describes the lessons learned from the implementation of a regional ensemble data assimilation and forecast system during the intensive observing period of the Remote sensing of Electrification, Lightning, And Mesoscale/microscale Processes with Adaptive Ground Observations (RELAMPAGO) field campaign (central Argentina, November–December 2018). This system is based on the coupling of the Weather Research and Forecasting (WRF) model and the Local Ensemble Transform Kalman Filter (LETKF). It combines multiple data sources both global and locally available like high-resolution surface networks, AMDAR data from local aircraft flights, soundings, AIRS retrievals, high-resolution GOES-16 wind estimates, and local radar data. Hourly analyses with grid spacing of 10 km are generated along with warm-start 36-h ensemble-forecasts, which are initialized from the rapid refresh analyses every three hours. A preliminary evaluation shows that a forecast error reduction is achieved due to the assimilated observations. However, cold-start forecasts initialized from the Global Forecasting System Analysis slightly outperform the ones initialized from the regional assimilation system discussed in this paper. The system uses a multi-physics approach, focused on the use of different cumulus and planetary boundary layer schemes allowing us to conduct an evaluation of different model configurations over central Argentina. We found that the best combinations for forecasting surface variables differ from the best ones for forecasting precipitation, and that differences among the schemes tend to dominate the forecast ensemble spread for variables like precipitation. Lessons learned from this experimental system are part of the legacy of the RELAMPAGO field campaign for the development of advanced operational data assimilation systems in South America.

1. Introduction

Over the last years, the most important operational centers in the world have implemented global numerical weather prediction (NWP) models with horizontal grid spacings ranging between roughly 7 and 20 km (Geer et al., 2018). In general, they also run regional domains using grid spacings from 1.3 to 15 km with data assimilation (DA) cycles of 1, 3, or 6 h (Gustafsson et al., 2018). These local forecasting systems can benefit from local observations such as radar and automatic weather station data, and can enable the computation of more frequent analyses in comparison with global cycles. It is worth mentioning that the positive impact of mesoscale and convective scale DA regional systems has

* Corresponding author at: CONICET (Consejo Nacional de Investigaciones Científicas y Técnicas), Argentina.
E-mail address: mdillon@smn.gov.ar (M.E. Dillon).

https://doi.org/10.1016/j.atmosres.2021.105858
Received 24 December 2020; Received in revised form 14 September 2021; Accepted 14 September 2021
Available online 25 September 2021

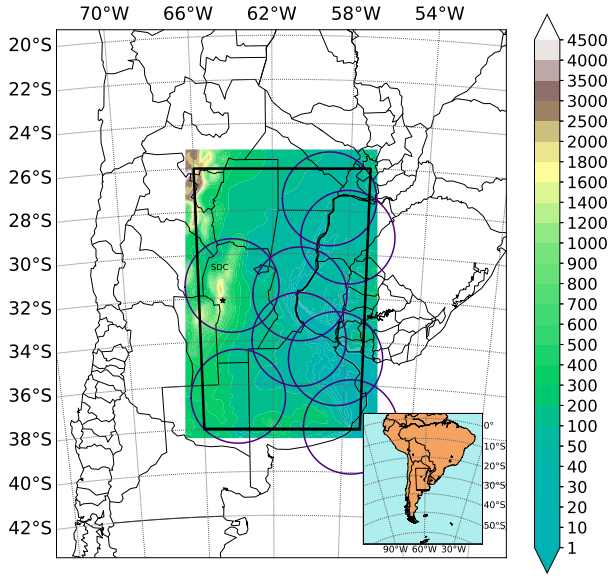

Fig. 1. RRR domain and topography (shaded) [m]. The circles indicate the 240 km radius of the eight radars assimilated. The black star refers to Villa Yacanto. SDC refers to Sierras de Córdoba mountain range. The black box indicates the area considered for validation. The lower-right subplot indicates the location of the verification domain within South America.

been documented among distinct geographical areas, showing that the quality of the forecasts initialized from these systems is significantly better than those produced by downscaling global analyses and forecasts (e.g., Xiao et al., 2005; Koizumi et al., 2005; Routray et al., 2010; Kuroda et al., 2012; Ferreira et al., 2017; Lien et al., 2017; Gustafsson et al., 2018; Zhu et al., 2019; Carrió et al., 2019). Regarding local observations, the assimilation of radar data was widely found to positively impact regional analysis and forecasts, as shown by Xiao et al. (2005), Routray et al. (2010), Putnam et al. (2017), and Gao et al. (2019), among many others.

Regional mesoscale DA systems have shown a positive impact on the precipitation forecasts of local severe weather using both variational and ensemble methods. For example, Routray et al. (2010) obtained an enhanced performance of the Weather Research and Forecasting (WRF) model with the 3D-VAR scheme for a monsoon case study employing 30 km horizontal grid spacing and assimilating Doppler weather radar data, and Kunii (2014) showed a positive performance of 12-km analyses applying the Local Ensemble Transform Kalman Filter (LETKF) system to a local severe rainfall event in Japan. Further, the U.S. National Weather Service runs the Rapid Refresh (RAP) regional operational hourly updated analysis and forecast system, using a 13-km hybrid ensemble-variational Gridpoint Statistical Interpolation (GSI) analysis system (Benjamin et al., 2016). Additionally, Pan et al. (2018) tested a prototype for the RAP forecasting system using a dual-resolution system consisting of a ~13-km hybrid system coupled with ensemble Kalman filter cycles at 40-km grid spacing.

Over South America, few studies have been documented regarding regional mesoscale and convective scale DA systems. Goncalves de Goncalves et al. (2015) presented experiments carried out at the Center for Weather Forecast and Climate Studies from the Brazilian National Institute for Space Research (CPTEC-INPE for their acronyms in Portuguese), using regional data assimilation cycles with 12, 9 and 3 km resolution, for one month. At the same time, promising results of DA applied to different case studies using resolutions between 1 and 10 km have been shown both in Brazil and Argentina (Ferreira et al., 2017; Bauce Machado et al., 2017; Toshio Inouye et al., 2017; Maldonado et al., 2019; Corrales et al., 2019; Vendrasco et al., 2020; Ferreira et al., 2020). At the time of writing, CPTEC is running a 5-km regional modeling system for South America using the WRF model with the GSI-DA system with a 6-h cycling interval (Sapucci personal communication[1]) and the Argentinian National Meteorological Service (ANMS) has been running a convective-scale downscaling forecast since 2016 (García Skabar et al., 2018), and is working actively in implementing a regional data assimilation system in order to improve the forecast of precipitation and severe weather events.

From June 2018 to April 2019, the Remote sensing of Electrification, Lightning, And Mesoscale/microscale Processes with Adaptive Ground Observations (RELAMPAGO) field campaign took place in central Argentina, with an Intensive Observing Period (IOP) during Nov-Dec 2018 to study extreme thunderstorms in the region (Nesbitt et al., 2021). Given the regional advances in DA, the positive performance of a coarser-resolution LETKF-WRF system over Argentina (Dillon et al., 2016), and the opportunity of running numerical experiments in real-time to support IOP operations during RELAMPAGO, a rapid-refresh mesoscale data assimilation and forecast system was designed. The RELAMPAGO Rapid Refresh (RRR) is a 10-km resolution, multi-physics ensemble-based, LETKF-WRF DA system developed as a joint effort among many institutions. This ensemble rapid-update-cycle system assimilates conventional, satellite, and radar observations, and is the first mesoscale DA system ever run in real-time in Argentina, providing the first set of analyses available to be used in research activities. For example, Pal et al. (2021) recently documented encouraging results using RRR simulations for the WRF-Hydro data forcing for the study of a hydrometeorological flash flood event.

This article describes in detail the RRR configuration and provides the first evaluation of its performance. Moreover, an analysis of the skill associated with the multi-physics approach used to run the different ensemble members is provided. The paper is organized as follows: the data assimilation and forecast system is described in Section 2, while the verification of different aspects of the RRR, including its analyses and forecasts impact, are shown in Section 3. Some insights regarding the different model configurations are given in Section 4. Finally, conclusions are summarized in Section 5.

2. Methodology

2.1. Data assimilation and forecast system

The RELAMPAGO Rapid Refresh ensemble-based data assimilation and forecast system was implemented in real-time during the RELAMPAGO field campaign as an experimental system. It consists of an hourly assimilation cycle and a 36-h ensemble forecast initialized every 3 h. The system was started at 01 UTC 5 November 2018 and continuously ran until 12 UTC 19 December 2018 (44 days) which coincides approximately with RELAMPAGO IOPs. The National Center for Atmospheric Research (NCAR) supercomputer Cheyenne (Computational and Information Systems Laboratory, 2019) was used to run the system. Graphical products were available in real-time at RELAMPAGO's operation center throughout the campaign at NCAR Earth Observing Laboratory Field Catalog.[2]

The RRR is based on the Weather Research and Forecasting Model (WRF; Skamarock et al., 2008), with its Advanced Research WRF dynamical solver (ARW) version 3.9.1.1, run with a 10-km horizontal grid spacing over a domain of 150 × 100 grid points using a Lambert projection (Fig. 1). The model top is set at 50 hPa, and the number of vertical sigma-p levels is 50.

The RRR uses a 60-member multi-physics and perturbed boundary conditions approach in which land-surface processes, microphysics, and radiation schemes are the same for all ensemble members. The multi-

[1] See products in https://previsaonumerica.cptec.inpe.br/wrf

[2] http://catalog.eol.ucar.edu/relampago/model see RRAA for analyses and RRAF for forecasts

Table 1
Generation of the 60-member RRR multi-physics ensemble as a combination of Cumulus and PBL parameterizations, and GEFS members for boundary conditions.

PBL Cumulus	YSU	MYJ	MYNN2
KF	1, 6, 8, 10, 15, 17, 19	2, 4, 9, 11, 13, 18, 20	3, 5, 7, 12, 14, 16
BMJ	2, 7, 9, 11, 16, 18, 20	1, 3, 5, 10, 12, 14, 19	4, 6, 8, 13, 15, 17
GF	1, 3, 8, 10, 12, 17, 19	2, 4, 6, 11, 13, 15, 20	5, 7, 9, 14, 16, 18

Table 2
GFS/GEFS initializations used for the boundary conditions needed to compute each RRR analyses.

GFS/GEFS initializations	RRR analyses
00 UTC	03, 04, 05, 06, 07, 08 UTC
06 UTC	09, 10, 11, 12, 13, 14 UTC
12 UTC	15, 16, 17, 18, 19, 20 UTC
18 UTC	21, 22, 23, 00, 01, 02 UTC

physics approach is introduced in order to represent the uncertainty associated with the parameterization of unresolved physical processes. This approach has been shown to produce more reliable ensembles in the context of regional data assimilation (Ha et al., 2015; Houtekamer and Zhang, 2016; Dillon et al., 2016). The Noah–MP land surface model was used (Niu et al., 2011); microphysics processes were parameterized with the WRF single-moment 6–class scheme (WSM6; Hong et al., 2006a), and radiation with the RRTMG shortwave and longwave scheme (Iacono et al., 2008). We used three different schemes to represent moist convection and planetary boundary layer (PBL) processes. For the former, the Kain–Fritsch scheme (KF; Kain, 2004), the Betts–Miller–Janjic scheme (BMJ; Janjić, 1994), and the Grell–Freitas scheme (GF; Grell and Freitas, 2013) were used. For the latter, the Yonsei University scheme (YSU; Hong et al., 2006b); the Mellor–Yamada–Janjic scheme (MYJ; Janjić, 1994), and the Mellor–Yamada Nakanishi Niino scheme (MYNN2; Nakanishi and Niino, 2009) were used.

It is worth noting that the multi-parametrization approach is used in the hourly forecasts needed for the assimilation and in the 36-h forecasts.

Both lateral and lower boundary conditions were taken from the 20 members of the National Centers for Environmental Prediction (NCEP) Global Ensemble Forecasting System v.11 (GEFS; Zhou et al., 2017) analyses and forecasts, available at 0.5° resolution, which were re-centered around the GFS higher resolution deterministic run, available at 0.25°, using linear interpolation. With the aim of enlarging the ensemble spread, these 20 boundary conditions were mixed with the nine different model configurations resulting from the combination of cumulus and PBL schemes as shown in Table 1. For example, the members with the KF-YSU parameterizations were combined with the GEFS members number 1, 6, 8, 10, 15, 17 and 19.

In order to attain a semi-operational schedule, the computation of the analysis was started 2 h after the corresponding analysis time. Boundary conditions for the RRR were always taken from the latest available GFS and GEFS runs, which are typically 4 and 5 h after the analysis time, respectively. Taking this into account, the initialization time corresponding to the boundary conditions used for each RRR cycle are summarized in Table 2.

The RRR analysis step is based on the four-dimensional Local Ensemble Transform Kalman Filter (4D-LETKF; Hunt et al., 2007; Miyoshi and Aranami, 2006; Miyoshi and Kunii, 2012a). In this approach an assimilation window is defined and forecast and observations distributed within this window are compared at the right time. Sample covariances derived from the ensemble are used to describe temporal and spatial covariances among different variables (i.e. an adjoint model is not required for the computation of the analysis). In this work we use a data assimilation window of 1 h divided into 10-min time slots used to compare the observations with the model output at the closest time. For each slot, all observations are assumed to be taken at the center of the interval. The assimilation window starts at the time of the previous analysis and up to the time of the current analysis (Fig. 2). Given the short length of the assimilation window, no temporal localization is used. RRR soil states were cyclically updated with the information from the GEFS ensemble members, re-centered around the GFS, through the *da_update_bc* utility from the WRF Data Assimilation package (WRFDA; Barker et al., 2012).

To reduce the impact of sampling errors and errors associated to non-linearities and also to account for model errors (not accounted for by the use of the multi-physics approach), a relaxation to prior spread inflation (RTPS; Whitaker and Hamill, 2012) is used with an alpha of 0.8, as in Necker et al. (2020). Sampling errors also lead to noise in the estimation of error covariances which is how the Kalman filter propagates the information among different variables. To mitigate this effect, the covariance matrix was localized in space using an R-localization method (Greybush et al., 2011). A single horizontal localization radius of approximately 180 km was implemented for all the observations, while

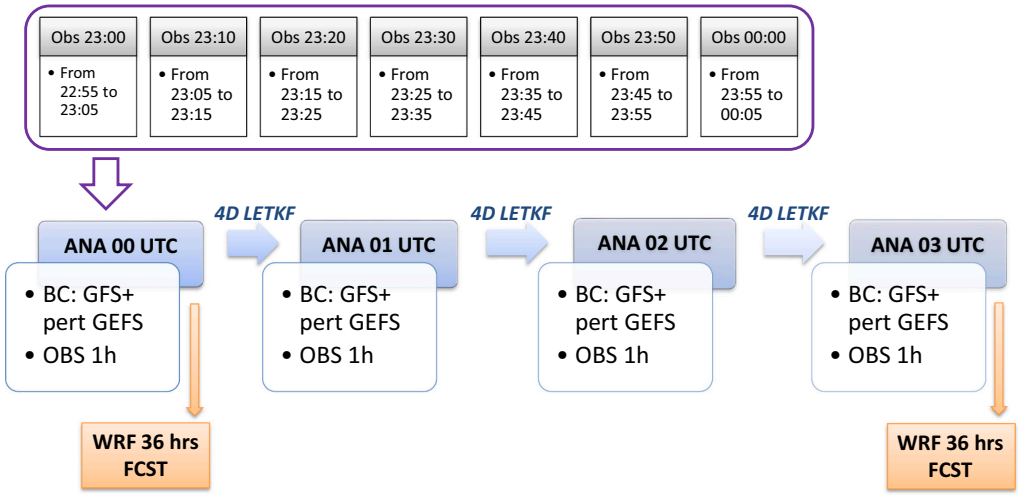

Fig. 2. Flow diagram of the RRR showing the hourly analysis generation (ANA) using 4D-LETKF and the 36 h forecasts generation every 3 h (FCST). "BC" stands for Boundary Conditions and OBS stands for observations. An example of the distribution of the observations within the assimilation window is shown for the 00 UTC analysis. See the text for more details.

Table 3
Characteristics of the assimilated observations: The acronym for each observation type, its data source, and the associated assimilated variables error magnitude [temperature (T), zonal (U) and meridional (V) wind components, surface pressure (PSFC), relative humidity (RH), specific humidity (Q), reflectivity (Z)]. *Please see the text for a detailed explanation of the errors.

Observation type	Data source	Assimilated variables error					
		T	U, V	PSFC	RH	Q	Z
		(K)	(ms^{-1})	(Pa)	(%)	($g\ kg^{-1}$)	(dBZ)
CSWS	ANMS Conventional Surface Weather Stations	2	1.4	160	10	–	–
ASWS	Automatic Surface Weather Stations	2	1.4	160	10	–	–
RS*	Radiosondes	1	variable	–	10	–	–
AIRPL	Airplanes	–	3.6	–	–	–	–
AIRSR*	NASA Atmospheric Infrared Sounder Retrievals	variable	–	–	–	variable	–
RADAR	C-band radar	–	–	–	–	–	5
GDMW	GOES Derived Motion Winds	–	7.5	–	–	–	–
SHBU	Ships, Buoys	2	–	–	–	–	–

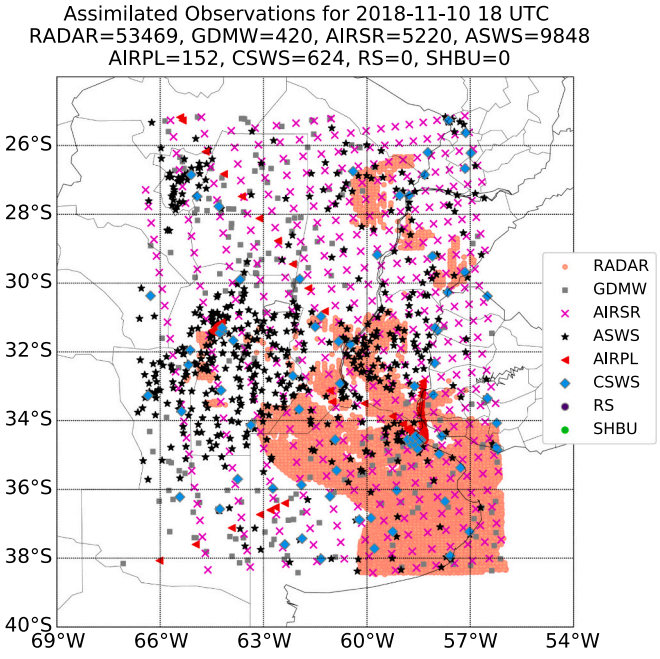

Fig. 3. Spatial distribution of different observations assimilated in the RRR on 10 November 2018 at 18 UTC. See Table 3 for a description of the different observation types. The total amount of assimilated observations for each data type is also indicated at the top.

a dual vertical localization was used for radar data (~ 7.3 km) and conventional observations (~ 12.5 km). A gross error check was also implemented to reject observations whose distance from the first guess was more than 10 times larger than the observation error.

2.2. Assimilated observations

Several observation types are assimilated into the RRR system. Their characteristics are summarized in Table 3, an example of the spatial distribution of the observations for 18 UTC 10 November is provided in Fig. 3, and Fig. 4 provides a summary of the observation count for each assimilation cycle. A brief description of the data sets and the pre-processing procedures are provided below.

- Conventional Surface Weather Stations (CSWS): These observations are provided by the ANMS and correspond to the Argentina, Uruguay and Paraguay surface operational networks. While their spatial distribution is heterogeneous, most of the 81 CSWS report hourly. Nevertheless, an increment of assimilated observations is detected at 00, 06, 12 and 18 UTC, considering the whole period.
- Automatic Surface Weather Stations (ASWS): These observations consists of 757 stations integrating 17 public and private surface networks. Observation providers and their website is listed in Appendix A. This data set is available through the RELAMPAGO Data Archive. The amount of assimilated observations from ASWS is notably larger than those assimilated from CSWS (27.93% versus 1.57% with respect to the total data assimilated).
- Radiosondes (RS): This data is also provided by the ANMS. There are radiosondes only at 00 UTC and 12 UTC over the domain in up to seven different locations.

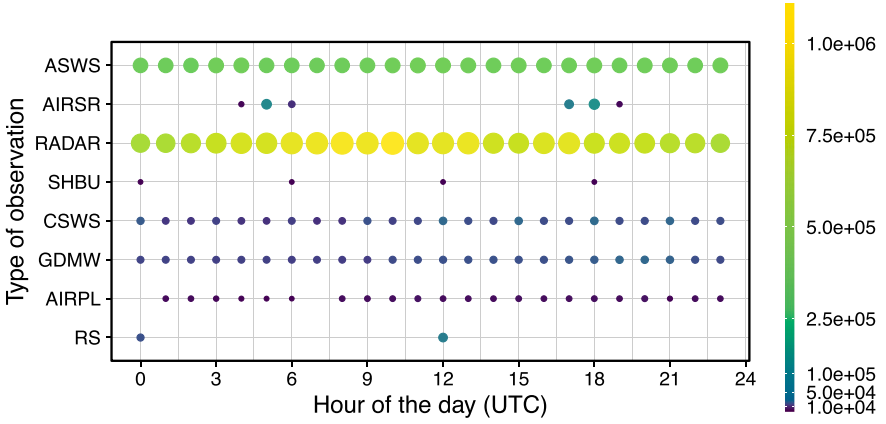

Fig. 4. The total number of each observation type assimilated for each hour of the day [UTC] for the validation period (from 00 UTC 9 November to 12 UTC 19 December 2018).

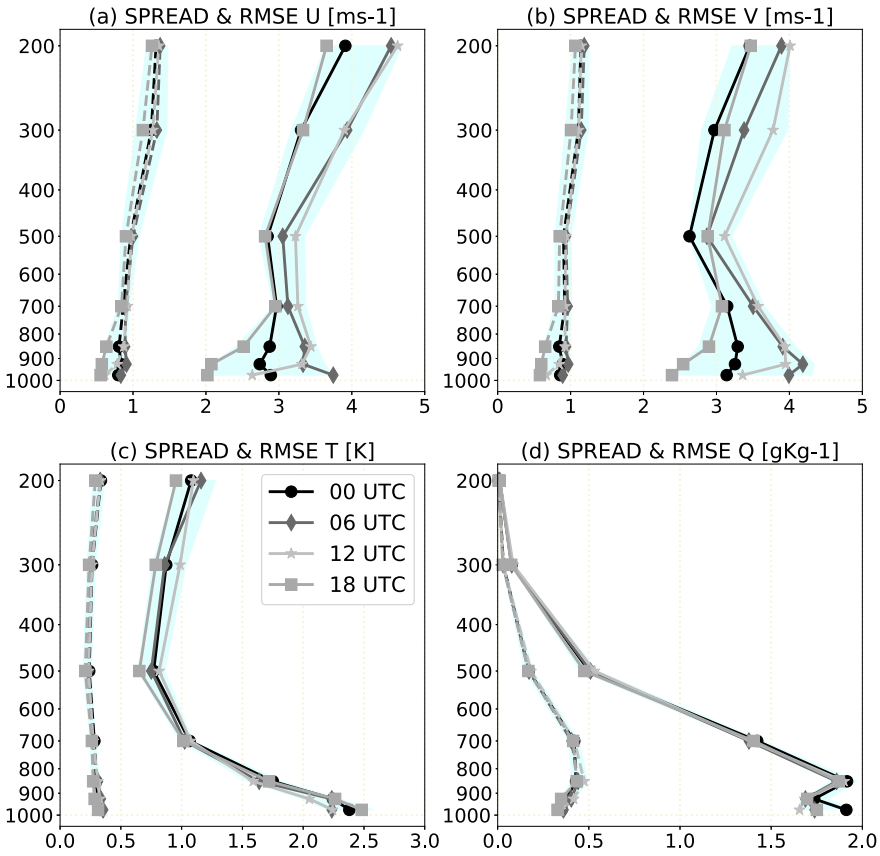

Fig. 5. Vertical profiles of the spatially averaged SPREAD (dashed lines) and RMSE with respect to ERA5 (solid lines) for (a) zonal wind component [ms^{-1}], (b) meridional wind component [ms^{-1}], (c) temperature [K], and (d) specific humidity [gKg^{-1}]; at 00, 06, 12, and 18 UTC. The shaded area illustrates the range of the profiles across the different hours of the day, for both SPREAD and RMSE.

- Airplanes (AIRPL): Provided by the ANMS. These observations do not cover the whole aircraft routes because we only considered the Aircraft Meteorological Data Relay (AMDAR) messages. Only wind data was assimilated.
- AIRS Retrievals (AIRSR): The Atmospheric Infrared Sounder (AIRS) is on board the National Aeronautics and Space Administration (NASA) Aqua polar-orbiting satellite. Near real time vertical profiles of estimated temperature and specific moisture retrievals (Susskind et al., 2014) are available through https://discnrt1.gesdisc.eosdis.nasa.gov/data/Aqua_AIRS_NRT/AIRS2RET_NRT.006. RRR analyses incorporates these profiles at its original horizontal and vertical resolution of approximately 45 km and 1 km, respectively. Only data below 200 hPa and with the best quality control flag are assimilated, following Tobin et al. (2006). Although these profiles are available only at specific hours (i.e., early morning and afternoon) and not everyday due to the satellite polar orbit, they represent a valuable data set that complements the sparse upper air network over the region and which have been successfully assimilated in regional systems over the world (e.g. Miyoshi and Kunii, 2012b; Dillon et al., 2019).
- C-band Radar Reflectivity (RADAR): This data is provided by the recently developed Argentine C-band Doppler dual-polarization weather radar network (de Elía et al., 2017). The RRR assimilates data from eight radars independently, as a mosaic product was not available (see Fig. 1 for their location and spatial coverage). Quality control is performed to the data to remove echoes associated with clutter, speckle, anomalous propagation, interference and complex terrain (Arruti et al., 2021). Areas strongly affected by attenuation are also identified and removed from the data. The quality control is performed in the original radar geometry. A superobbing is performed to convert the data from its original resolution (which can be as high as 500 m) to an horizontal resolution of 10 km, a vertical resolution of 1 km, and a time resolution of 10 min, consistent with the model resolution and output frequency. Clear air observations of reflectivity (i.e., reflectivity observations lower than 0 dBZ) were assimilated to suppress spurious convection within the computational domain (Tong and Xue, 2005; Aksoy et al., 2009). Note the large quantity of radar data in comparison with other sources (67.53%), due to the inherent resolution of this kind of data. Radial velocity observations were not assimilated in this experiment since quality control to properly handle this particular data type was not yet available at the ANMS.
- GOES Derived Motion Winds (GDMW): Motion vectors estimated from the water vapor, visible, and infrared channels from the Geostationary satellite GOES-16 (Derived Motion Winds) are assimilated in the RRR. Given that sometimes the horizontal resolution of these motion vectors can be very high, a superobbing technique is applied with an horizontal resolution of 30 km and a vertical resolution of 25 hPa. Only the data that passed the NCEP quality control were used in the superobbing. To access the data in real time the NOAA-NESDIS PDA (Product Distribution and Access) system was used through the ANMS. The GDMW were assimilated with an hourly frequency.
- Ships and Buoys (SHBU): This data is provided by the ANMS. Although the sea surface area in our domain is small, we were able to assimilate some SHBU data at 00, 06, 12, and 18 UTC.

Observation errors for CSWS, ASWS, RS, AIRPL and SHBU were set following the values recommended in the WRFDA package (Table 3). Particularly, for RS the errors are a function of height. Observational

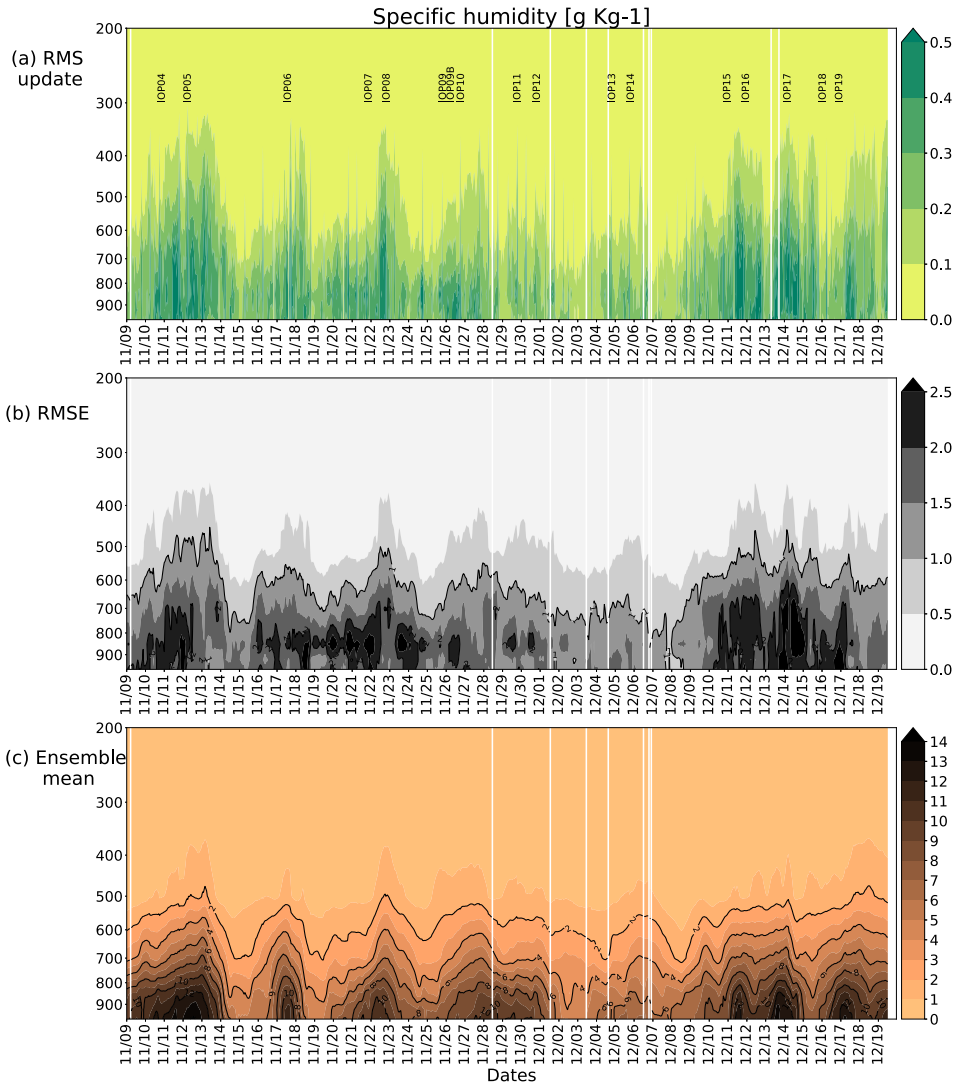

Fig. 6. Time height cross section of: (a) RMS of the ensemble mean analysis update, (b) RMSE of the ensemble mean analysis with respect to ERA5 and (c) ensemble mean analysis, of the specific humidity [gKg^{-1}]. The corresponding RELAMPAGO IOP missions starting time are also indicated.

errors for GDMW and AIRSR are specified by the data provider (*TAirStdErr* and *H2OMMRStdErr* for temperature and specific moisture, respectively), while an error of 5 dBZ is assumed for superobbed radar reflectivity data based on previous works (e.g. Tong and Xue, 2005; Lange and Craig, 2014; Jones et al., 2015).

All the observations were collected and pre-processed in real time (considering a 90 min cutoff) at the ANMS and then transferred to Cheyenne supercomputer to be assimilated. It is worth mentioning that the integration of ASWS was feasible through RELAMPAGO efforts, enabling for the first time this kind of data for assimilation and forecast verification over the region. Regarding the observations collected during the field campaign, they were not considered for the RRR as it would be difficult to receive and process them in real time. Nevertheless, a project to evaluate the impact of the assimilation of the data collected during the campaign is underway.

Comparing these data sets with the ones used for the assimilation in the global model, RADAR and ASWS stand out in the regional system while the other observation types are included in both RRR and GFS. Note that the global model also incorporates the radiances of multiple sensors, which is a great advantage.

2.3. Validation

In order to evaluate the performance of the ensemble based data assimilation and forecast system presented in this article, the following data sets were considered as reference atmospheric states.

- Hourly ERA5 reanalyses of 0.25° resolution (Hersbach and Dee, 2016) of zonal (U) and meridional (V) wind components, temperature (T) and specific humidity (Q). For comparison with this data set, the RRR analyses and forecasts were linearly interpolated to the ERA5 regular grid.
- Data collected from surface stations (CSWS and ASWS) of 2 m temperature (T2m) and 10 m winds (U10m and V10m). For comparison, RRR forecasts were linearly interpolated to the observation locations.
- Satellite precipitation estimation IMERG Final Run at 0.01° resolution (Huffman et al., 2018). For comparison, the RRR forecasts were linearly interpolated to the IMERGFR regular grid.
- Multi-Network Composite Highest Resolution Radiosonde Data (UCAR/NCAR, 2020) at Villa Yacanto (Fig. 1) providing vertical profiles of U, V, T and dewpoint (Td). For comparison, the forecasts

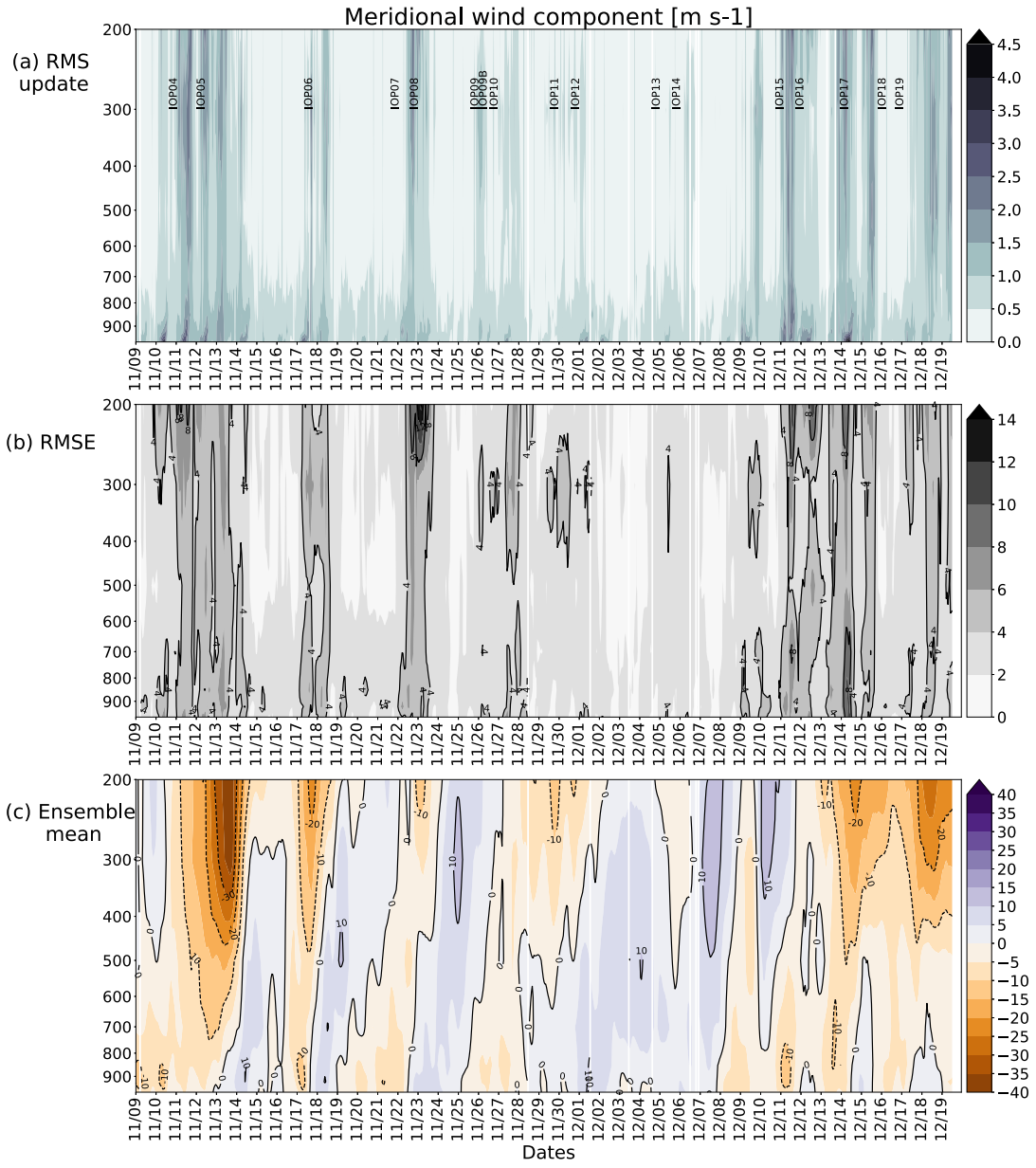

Fig. 7. As in Fig. 6 but for the meridional wind component [ms^{-1}].

were interpolated to the location of the observation using a closest neighbor approach.

Villa Yacanto, located eastward of the highest peak of Sierras de Córdoba (SDC) with an altitude of 1161 m above mean sea level, is one of the nine fixed sounding sites considered for the campaign (Schumacher et al., 2021). Radiosondes launched at 00, 12, 15, 18 and 21 UTC are used for this verification as a preliminary exploration. A validation of RRR using both mobile and fixed soundings along with other data sets collected during RELAMPAGO will be assessed in a future work.

The following measures were used for the validation of the analysis and forecasts. The Root Mean Square Error (RMSE) and the BIAS were calculated considering either the spatial or the time dimensions. In eqs. 1 and 2, O and X stand for the reference and simulated atmospheric states, respectively, while the subscript $i \in \{1,\ldots,N\}$ represents different observation locations and/or different times.

$$RMSE = \sqrt{\frac{1}{N}\sum_{i=1}^{N}(X_i - O_i)^2} \tag{1}$$

$$BIAS = \frac{1}{N}\sum_{i=1}^{N}(X_i - O_i) \tag{2}$$

Also, the ensemble spread (SPREAD) was computed following the considerations of Fortin et al. (2014) to compare this quantity with the RMSE of the ensemble mean, which is desired to be equal. In eq. 3, $\overline{X}$ represents the ensemble mean, and X_k stands for the $k \in \{1,\ldots,M\}$ ensemble member.

$$SPREAD = \sqrt{\frac{1}{N}\sum_{i=1}^{N}\frac{1}{M-1}\sum_{k=1}^{M}\left(\overline{X}_i - X_{k,i}\right)^2} \tag{3}$$

The Fractions Skill Score (FSS) was used for the validation of precipitation forecasts following Roberts (2008). The original formulation

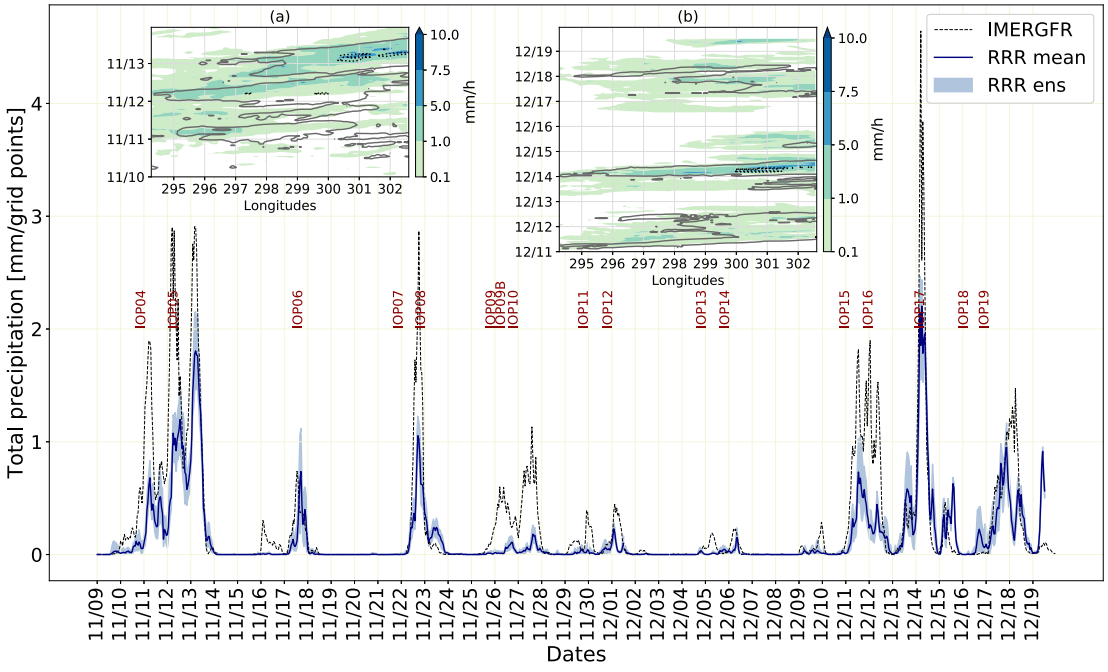

Fig. 8. Temporal evolution of the hourly accumulated precipitation averaged over 29–35°S and 66–57°W [mm/grid points], for the RRR first guess ensemble mean (solid line), the RRR ensemble range (shaded), and the IMERGFR (dashed line). The corresponding RELAMPAGO IOP missions starting time are also indicated. Subplots (a) and (b) show the Hovmöller diagram of hourly precipitation for the 10–13 November and 11–19 December periods, respectively, for the RRR ensemble mean (shaded) and the IMERGFR [1 mmh^{-1} (filled contour) and 7.5 mmh^{-1} (dashed contour)].

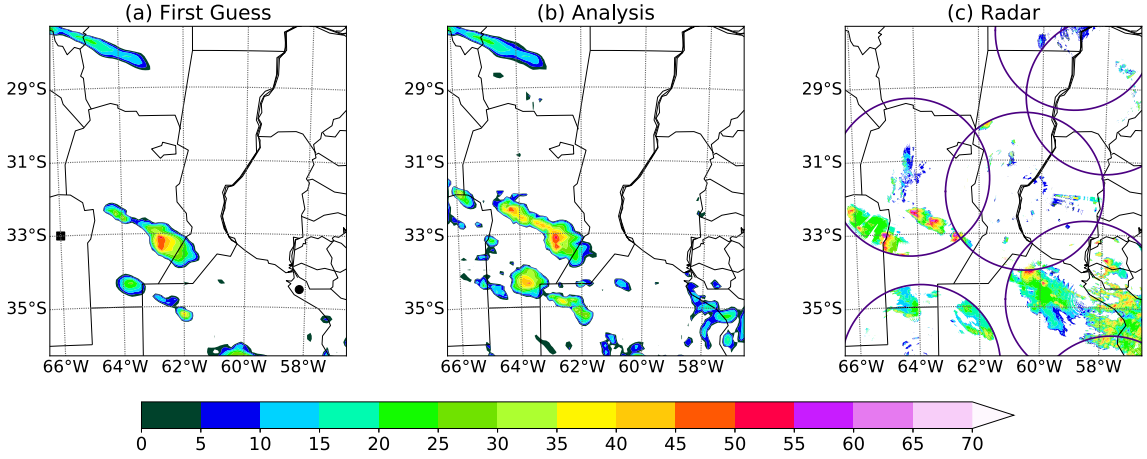

Fig. 9. Maximum reflectivity [dBZ] distribution in the (a) RRR first guess ensemble mean, (b) RRR analysis ensemble mean and (c) observed by the C-band radar network; for 14 December at 00 UTC. In (a) the black square and dot refer to San Luis Province and La Plata River, respectively. The 240 km radius circles from the radars are also depicted in (c).

was slightly modified to take into account the information provided by all the ensemble members as in Maldonado et al. (2021). The modified version of the score is defined as:

$$FSS = 1 - \frac{\frac{1}{M}\sum_{j=1}^{M}\left([P_x]_j - P_{oj}\right)^2}{\frac{1}{M}\sum_{j=1}^{M}\left([P_x]_j\right)^2 + \frac{1}{M}\sum_{j=1}^{M}\left(P_{oj}\right)^2} \quad (4)$$

where $[P_x]$ is the ensemble-based probability of the accumulated precipitation being over a certain threshold, spatially averaged over a squared box of size *LxL* grid points; and P_o is the spatially observed frequency of precipitation over the same threshold computed over the same box. The subscript $j \in \{1,\ldots,M\}$ identifies the individual boxes, with M the total number of boxes considered. This score is typically computed for a range of box sizes and precipitation thresholds to describe forecast skill as a function of the horizontal scale and precipitation intensity. In this work we apply this score for the verification of 6-h accumulated precipitation forecasts.

Analysis and forecast verification was performed over the domain 66–57°W and 26–38°S (cf. black box in Fig. 1) to avoid the effect of the boundaries. A 40-day verification period from 00 UTC 9 November to 12 UTC 19 December 2018 was considered, allowing the system approximately a 4-day spin up period (~95 DA cycles). The total number of DA cycles in the study period is 964, as 8 of them were lost due to issues with data storage and transfer.

For the 36 h ensemble forecasts validation, in addition to those initialized from the LETKF-WRF cycles, a 60-member WRF ensemble

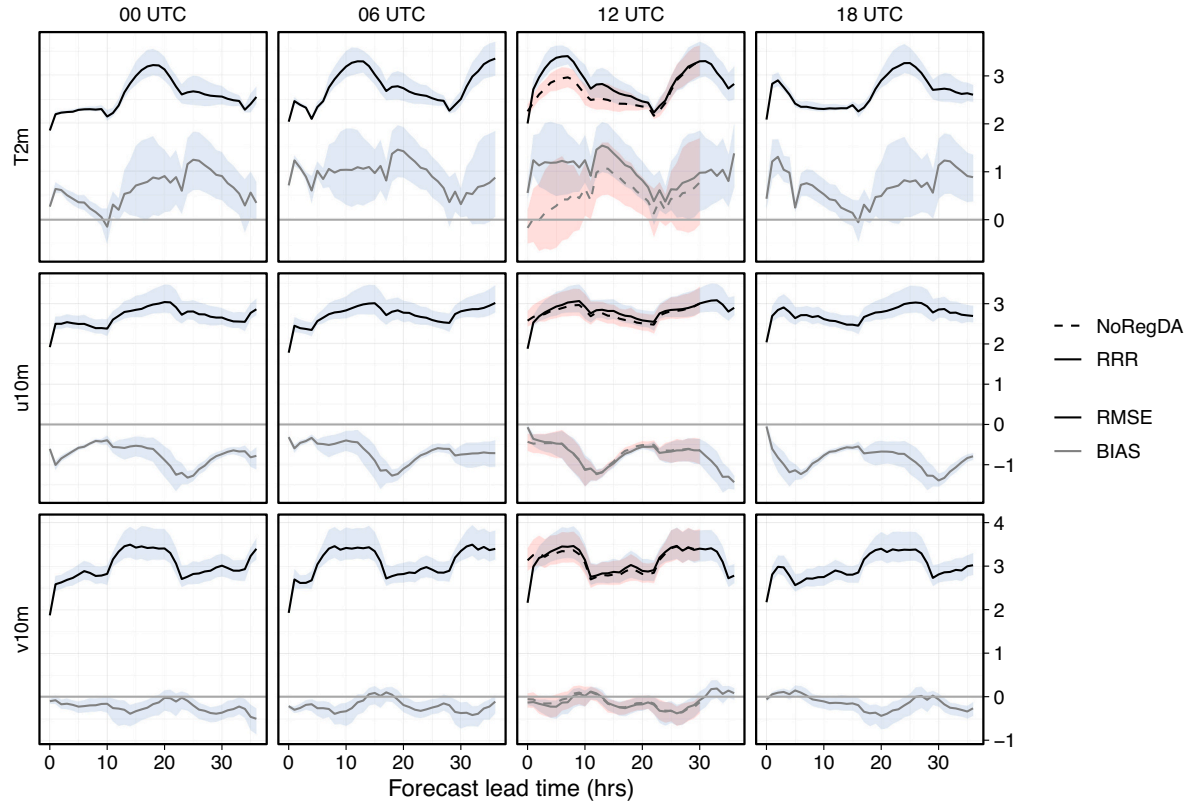

Fig. 10. Ensemble mean forecast RMSE (black lines) and BIAS (grey lines) with respect to CSWS and ASWS observations as a function of the forecast lead time. The light blue shaded indicates the range of RMSE and BIAS across the RRR ensemble members. Each column correspond to a different initialization time at 00, 06, 12 and 18 UTC, and each row to a different variable: T2m [K], U10m [ms^{-1}] and V10m [ms^{-1}]. The NoRegDA ensemble RMSE and BIAS (dashed contours) as well as their corresponding range across ensemble members (pink shaded) are included for the 12 UTC initialization time. RMSE and BIAS are averaged over the validation domain and over all the forecasts within the validation period. (For interpretation of the references to colour in this figure legend, the reader is referred to the web version of this article.)

without LETKF application (i.e., a cold-start ensemble) was also run during the same period, considering the configuration described in Table 1. Only the 36 h forecasts initialized at 06 UTC were computed. This experiment was called NoRegDA because no regional data was assimilated, but the ensemble still benefits from the global data assimilation system. The 06 UTC NoRegDA forecasts are compared with the RRR forecasts initialized at 12 UTC since these two forecasts use the same lateral and lower boundary conditions (cf. Table 2).

3. Overview of the RRR performance

3.1. Analysis and first guess

The vertical profiles of the spatially averaged SPREAD and RMSE of the analysis mean with respect to ERA5 are shown for 00, 06, 12, and 18 UTC in Fig. 5. At low levels for both wind components, the time with the smallest RMSE is 18 UTC (3 p.m. local time) while the one with the biggest errors is 06 UTC (3 a.m. local time). The meridional wind RMSE profiles present a local maximum at low levels during the night and early morning (from 00 to 12 UTC). This pattern may be associated with a misrepresentation of the Low Level Jet (LLJ), which shows its maximum intensity at these times and is frequently present over the northern half of the RRR domain during the summer season (Vera et al., 2006). Regarding temperature and specific humidity, their RMSE show a diurnal cycle in the lowest level evaluated (975 hPa): the smaller errors correspond to 06 and 12 UTC for temperature, while 12 UTC is the time of less error for humidity. In addition, a diurnal cycle is encountered for T, U and V at upper levels, which may be related to the distribution of the distinct type of data assimilated along the day (Fig. 4). The profiles of the remaining hours of the day offer similar characteristics for the four variables evaluated, as it can be seen by the shaded areas in Fig. 5.

One evident feature is the under-dispersion of the ensemble as the SPREAD is lower than the RMSE for all the variables, which was also shown by Dillon et al. (2019), for a 40 km LETKF-WRF over Southern South America. Nevertheless, it should be noted that ERA5 errors are embedded in RMSE calculation, contributing to increase the observed difference between the ensemble spread and the model error. Likewise, it is not possible to know accurately the impact of the reference data errors in the SPREAD-RMSE comparison.

It is worth mentioning that the RMSE values found for the RRR are similar to those reported for other regional DA systems. For example Lien et al. (2017) showed temperature RMSE values generally lower than 3 K over Japan with a regional 18-km LETKF system implemented with the SCALE model. They also showed annual RMSE mean values of 3.59 and 3.99 ms^{-1} for meridional and zonal wind components. The SPREAD-RMSE ratio for the zonal wind component at 300 hPa is also in agreement with our results (Lien et al., 2017).

To study the impact of the assimilated observations as the DA cycles progressed, the hourly evolution of the vertical profiles of different quantities are presented in Figs. 6 and 7: (a) the Root Mean Square (RMS) update of the ensemble mean analysis with respect to the ensemble mean first guess in model space (using the eq. 1), (b) the RMSE of the ensemble mean analysis with respect to ERA5, and (c) the ensemble mean analysis, for the specific humidity and the meridional wind component. The starting times of the RELAMPAGO IOPs are also indicated to let the reader easily have a first impression on the RRR performance for each event (please refer to the NCAR Earth Observing Laboratory Field Catalog for a detailed description of each IOP). One

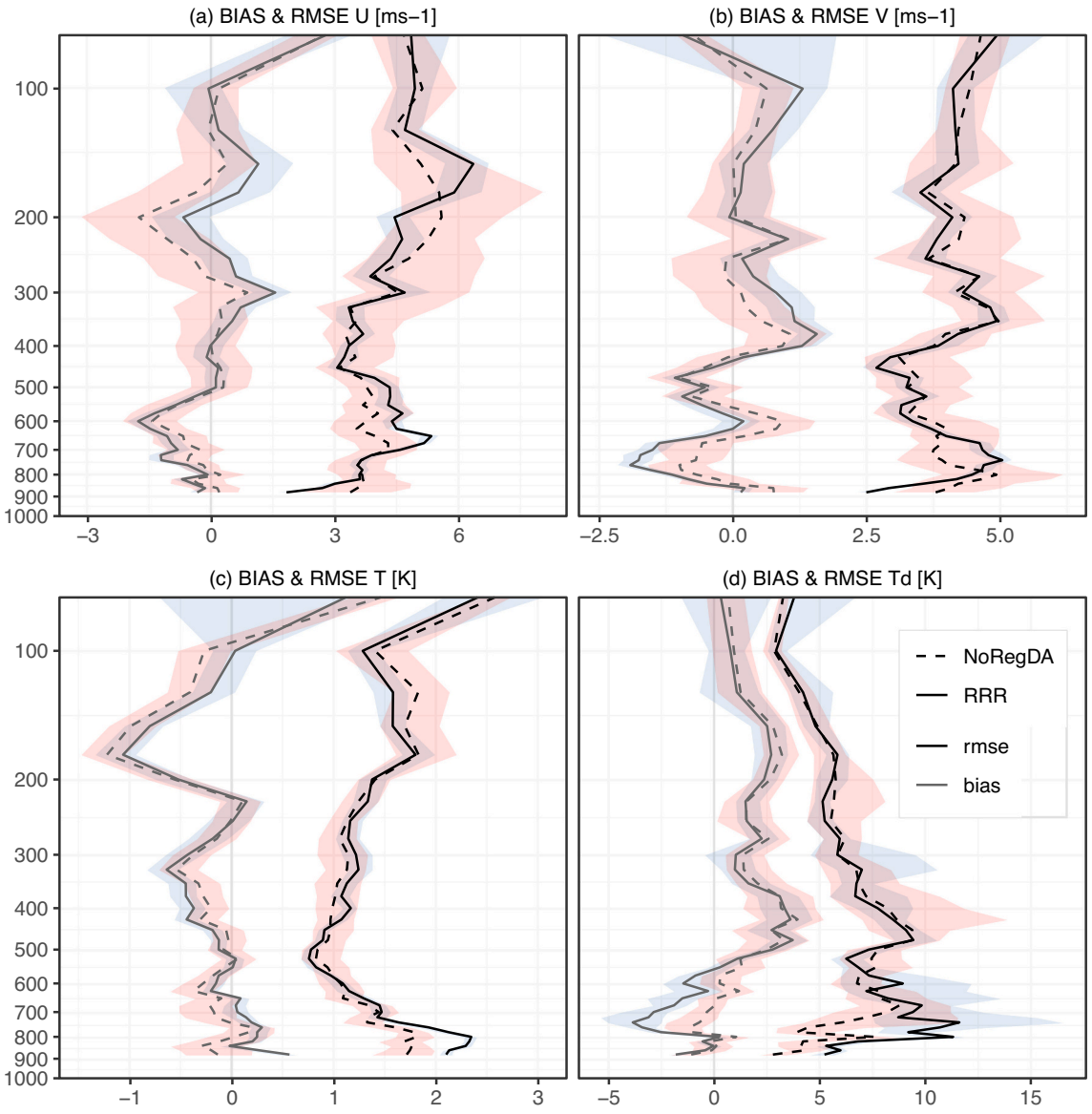

Fig. 11. Temporally-averaged ensemble mean forecast RMSE (black lines) and BIAS (grey lines) with respect to Villa Yacanto radiosondes valid at 12 UTC for: (a) zonal wind component [ms^{-1}]; (b) meridional wind component [ms^{-1}]; (c) temperature [K]; (d) dewpoint [K]. The light blue shaded indicates the range of RMSE and BIAS across the RRR ensemble members (initialized at 12 UTC, 0 h forecast lead time). The NoRegDA ensemble RMSE and BIAS (dashed contours) as well as their corresponding range across ensemble members (pink shaded) are included (initialized at 06 UTC, 6 h forecast lead time). (For interpretation of the references to colour in this figure legend, the reader is referred to the web version of this article.)

remarkable aspect is that the filter ran in a stable way during the whole study period. The magnitude of the observation impact is strongly modulated by the domain averaged precipitation (Fig. 8) with the stronger corrections being made during the periods with larger precipitation rates. Also the errors are larger during rainy periods. This is also true for the temperature and the zonal wind component (not shown). Moreover, the RMS update generally shows a diurnal cycle with maximum values close to surface during the night for the wind, and during the afternoon and the night for the specific humidity and temperature.

In general, it was found that for all the variables the dates for the maximum RMSE (with respect to ERA5) are in concordance with the ones for the maximum RMS update. Observing the ensemble means, it can be shown that those dates also correspond with the presence of high amounts of humidity at low levels, with an attendant northward wind component. During the summer season, humid periods with prevailing northerly flow are characterized by higher convective instability. When this instability is released, error growing rates are significantly larger and therefore, faster departures of the forecast from the observations are expected. Also, previous studies (e.g. Ruiz et al. (2010)) documented systematic errors in the representation of intense low-level northerly flow associated with a southward extension of the South American LLJ. These systematic errors, that consists on a weaker simulated low level flow, can also contribute to the day-to-day changes in the magnitude of the analysis updates.

In Fig. 8 we present the temporal evolution of the hourly total precipitation per grid points computed in the domain 66–57°W and 29–35°S (note that this is a bit smaller in latitude than the black box indicated in Fig. 1), for the RRR first guess ensemble members and the ensemble mean (i.e. one hour forecasts), and for IMERGFR. Generally, the RRR represents all the events estimated by IMERGFR, although the precipitation amount is systematically lower.

Two particular periods (10–13 November and 11–19 December, containing IOPs 04–05 and 15–19, respectively) are displayed in more

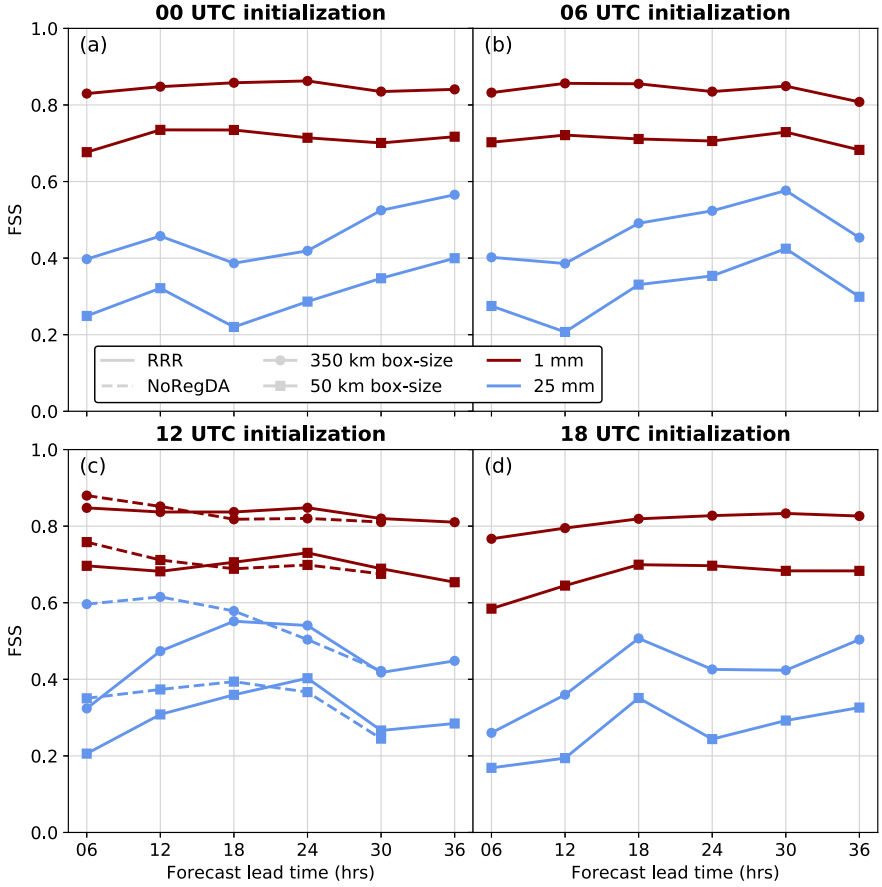

Fig. 12. 6 h accumulated precipitation fractions skill score (FSS) as function of forecast lead time, for thresholds of 1 mm (red line) and 25 mm (blue line), and box sizes of 50 km (squares) and 350 km (circles). RRR forecasts initialized at (a) 00 UTC, (b) 06 UTC, (c) 12 UTC and (d) 18 UTC. The NoRegDA experiment initialized at 06 UTC (dashed line) is included in (c). (For interpretation of the references to colour in this figure legend, the reader is referred to the web version of this article.)

detail using Hovmöller diagrams (Fig. 8a and b). Overall, the evolution of the estimated precipitation is well captured by the RRR, and likewise the location of the maxima.

To ilustrate the impact of radar observations, Fig. 9 shows the distribution of the maximum reflectivity in the mean first guess, the mean analysis and the observations for 14 December 00 UTC. There exists a clear improvement of the reflectivity around 34°S and 64°W between the first guess and the analysis. The systems over northern San Luis province and over La Plata river were not represented by the first guess, but do appear to some extent in the analysis. However, the DA system was not able to simulate the precipitating system near 34°S and 60°W. Probably the lack of availability of radar data in the trajectory of the system was an important cause of the misrepresentation of convection (not shown).

3.2. 36 h Ensemble forecasts

Surface variables were verified against ASWS and CSWS data. The scores of the U10m, V10m and T2m 36 h forecasts from four different initializations (00, 06, 12 and 18 UTC) are presented in Fig. 10. Generally, a positive BIAS is encountered for the temperature. Please note that a positive BIAS also dominates the analyses below 850 hPa with respect to ERA5 during the whole period (not shown), suggesting that the WRF model with the above mentioned configurations produces warmer low level temperatures.

In fact, a warm BIAS in T2m forecasts has been documented over central and eastern Argentina during one summer season, using a 40-km WRF with different parameterizations by Ruiz et al. (2010). In addition, the ANMS operational 4-km WRF generally overestimated T2m during 2020 in the region (Matsudo et al., 2021).

Regarding the winds, the BIAS is bigger in module for U10m than for V10m, which values are generally between 0 and − 0.5 ms^{-1}. A diurnal cycle of RMSE was identified for T2m and both wind components, with better scores during the night hours. These RMSE values are similar to those previously shown with different WRF configurations at surface (Ruiz et al., 2010) and at low levels (Dillon et al., 2016) over the region. Note that Benjamin et al. (2016) also found the smallest errors for 12 h surface variables forecasts during the night, using their RAP system over United States (which uses a 13-km WRF).

In relation to the NoRegDA statistics, for the temperature both the RMSE and BIAS generally perform better than RRR for the first 24 h. The BIAS in NoRegDA is close to zero at the beginning and increases along the forecast lead times, while in the case of RRR the BIAS is far from zero from the beginning. This behavior suggests that systematic errors in the WRF model accumulate during the data assimilation cycles, resulting in a biased initial condition.

For surface winds, the RRR performs better in terms of RMSE for the first 2–3 forecast hours but shows an afterwards rapidly increase. The reason for this rapid information loss provided by the observations for this particular variable is not clear and requires further investigation. For example, techniques incorporating a digital-filter initialization (as applied to RAP (Benjamin et al., 2016)) should be studied to reduce initial noise in the first forecast hour and therefore produce a more effective assimilation of the observations.

In Fig. 11 the vertical profiles of BIAS and RMSE with respect to Villa Yacanto radiosondes valid at 12 UTC are shown, using the 0 and 6 h forecast lead times for RRR and NoRegDA, respectively. For the wind components, the less RMSE values are encountered near surface while maximums are found around 650 and 750 hPa for U and V, respectively,

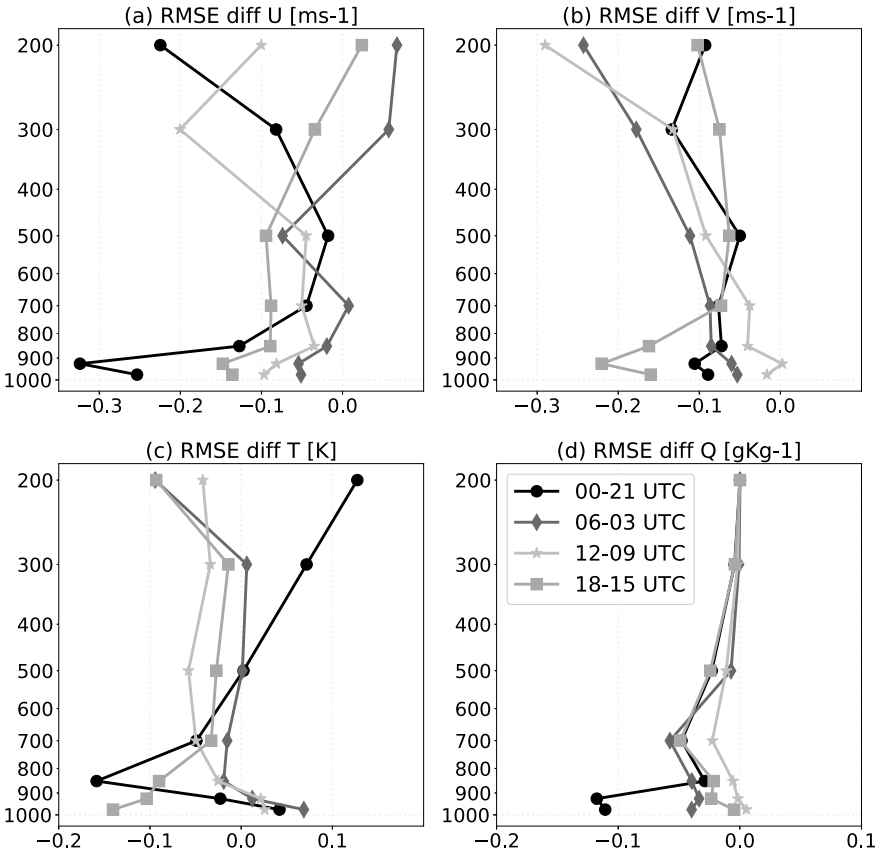

Fig. 13. Difference of RMSE with respect to ERA5 for RRR forecasts initialized at different cycles (00 minus 21 UTC; 06 minus 03 UTC; 12 minus 09 UTC; 18 minus 15 UTC) but driven by the same GEFS boundary conditions; for (a) zonal wind component [ms^{-1}]; (b) meridional wind component [ms^{-1}]; (c) temperature [K]; (d) specific humidity [gKg^{-1}]. The figure condensates the information of all members and forecasts lead times (see the text for more details in the calculation).

for RRR. Temperature errors above 2 K are registered below 800 hPa, associated to a low-level warm BIAS. Dewpoint errors up to 12 K evidence the model deficiencies in representing properly the humidity, with a dry (wet) BIAS below (above) 550 hPa. Note that a dry BIAS was also encountered for convection-permitting deterministic WRF for this location during the same period (Casaretto et al., 2021). In addition, mid level dry model BIAS was documented by Piersante et al. (2021) over the region using radiosonde data to validate a 20-km WRF simulation. In relation to the NoRegDA statistics, although its values are very close to RRR, its ensemble mean generally performs better for all these variables. Moreover, the NoRegDA ensemble spread is generally larger than the RRR one, in particular below 700 hPa. The great amount of ASWS assimilated observations (as mentioned in Section 2.2) may have impacted negatively in low levels RRR spread.

Regarding the precipitation, in Fig. 12 we present the FSS against IMERGFR precipitation estimates as a function of the forecast lead time. Overall, the 00 and 12 UTC initializations show better scores considering both the 1 and 25 mm 6 h accumulated thresholds, and the different scales analyzed. For the bigger threshold, the best FSS values are encountered at 12 UTC valid time (e.g. 18 and 30 h forecast lead times for 18 and 06 UTC initializations, respectively), while the worst values are detected at 18 UTC valid time (e.g. 6 and 18 h forecast lead times for 12 and 00 UTC initializations, respectively). This behavior suggests that the RRR is more skillful in forecasting morning than afternoon heavy precipitation. In addition, NoRegDA performs better, particularly for the 25 mm threshold and during the first 12 forecast hours, possibly because initial conditions provided by RRR are not as good as the ones provided by the global data assimilation system.

In order to evaluate the overall impact of the assimilated observations, we compute the spatially averaged RMSE for each forecast lead time of different initializations with respect to ERA5, for each member for distinct levels. Then we compare the errors between the initializations driven by the same GEFS boundary conditions (for example 09 and 12 UTC) considering the common valid times (for example 3–36 h 09 UTC forecasts versus 0–33 h 12 UTC forecasts). Finally, an average among the forecasts lead times and the ensemble members is taken to obtain one vertical profile to represent the RMSE difference for RRR forecasts initialized at different cycles (Fig. 13). Overall, negative values are encountered, suggesting that the observations assimilated in between are responsible for error reduction, as the same boundary conditions are used. However, there are some positive values, for example for low level temperature for three time pairs of day, except for the difference between the forecasts initialized at 18 and 15 UTC.

We perform a similar evaluation using Villa Yacanto radiosondes valid at 12 UTC (Fig. 14). In general, larger RMSE reductions are observed at middle and upper levels for all the variables, while at lower levels more positive values are found. At low levels the greatest improvements are registered at 00 UTC for T and at 18 UTC for U and V.

Further investigation is required to identify the observation types responsible for the detrimental impact upon the quality of the analyses and forecasts. Analyzing the diurnal cycle errors not only in this location but also in the other sounding sites, would help to understand both the DA strengths and weaknesses.

4. Insight on the multi-physics ensemble

In this section we evaluate the performance of the different PBL and cumulus parameterizations used in the ensemble (Table 1). To assess the impact of each PBL (cumulus) scheme, we analyze the three sub-ensembles that result from the combination with the cumulus (PBL)

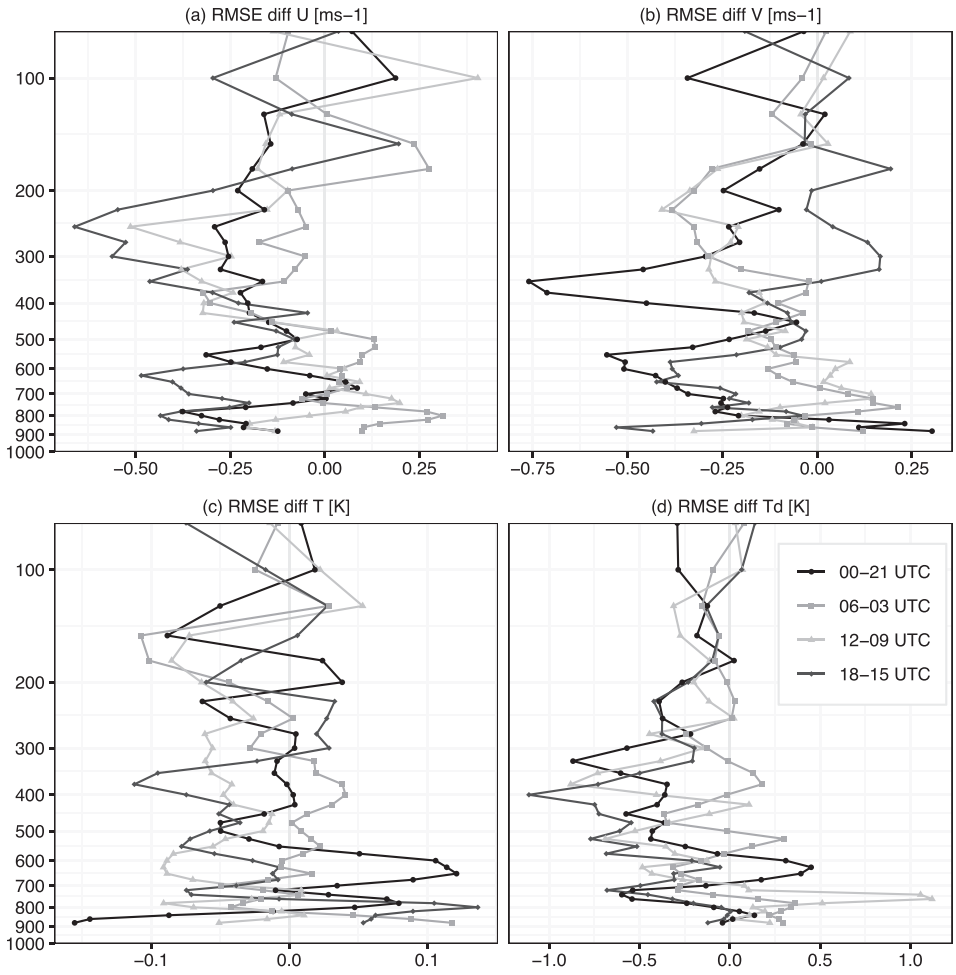

Fig. 14. Difference of RMSE with respect to Villa Yacanto radiosondes for RRR forecasts initialized at different cycles (00 minus 21 UTC; 06 minus 03 UTC; 12 minus 09 UTC; 18 minus 15 UTC) but driven by the same GEFS boundary conditions; for (a) zonal wind component [ms^{-1}]; (b) meridional wind component [ms^{-1}]; (c) temperature [K]; (d) dewpoint [K]. The figure condensates the information of all members and forecasts lead times (see the text for more details in the calculation).

schemes. For these sub-ensembles we compute the BIAS and RMSE for T2m and V10m, and the FSS for the 6 h accumulated precipitation.

For T2m and V10m a different behavior is detected for the PBL schemes RMSE when fixing a cumulus parameterization for forecasts initialized at 12 UTC (Figs. 15a, b and c). The largest RMSE corresponds to MYJ for the wind for all the forecast lead times (this is also true for the zonal component, not shown), but this PBL parameterization exhibits the largest errors for the temperature only during the day time. For the BIAS, MYJ shows the most positive values during warm hours, while during the night it is the scheme with less BIAS (in module). In addition, MYNN2 exhibits the BIAS closest to zero during the day time. The same behavior is presented for the forecasts initialized at 00, 06 and 18 UTC (not shown).

Cumulus parameterizations have an impact upon T2m which is as large as the one produced by different PBL schemes (Figs. 15d, e and f). This impact can be explained through the coupling between the cumulus scheme and the parameterization of radiative fluxes and also due to the direct low-level temperature tendencies associated with cumulus schemes. The impact on low-level winds is much smaller, as their tendencies are not directly modified by cumulus schemes and in this case the impact is indirect (e.g. through changes in the larger scale circulation or due to the development of mesoscale circulations like those associated with cold pools). Regarding the BIAS, more distinctions appear among the cumulus parameterizations: for the temperature generally GF shows the values closest to zero and for the wind both GF and KF perform better most of the time. Similar results were found for the forecasts initialized at 00, 06 and 18 UTC (not shown).

The FSS of precipitation, for the forecasts initialized at 00 and 12 UTC (Fig. 16) indicates that precipitation forecasts are, as expected, more sensitive to the choice of the cumulus parametrization than to the choice of the PBL scheme (as shown for example by Piersante et al. (2021)). Particularly, BMJ shows the worst performance for both thresholds. In the case of the PBL parameterizations, some distinctions appear at the 25 mm threshold, where MYJ is slightly better than YSU and MYNN2.

In addition, Hovmöller diagrams of hourly accumulated precipitation from forecasts initialized on 12 November at 12 UTC using different configurations are compared against IMERGFR in Fig. 17. Forecasted precipitation on each panel of Fig. 17 consists of the mean over the ensemble members that share that particular combination of cumulus and PBL schemes. The behavior of the precipitation for this specific case confirms the results obtained with the FSS: the greater differences occur among the cumulus schemes, with BMJ showing the worst performance as it significantly underestimates precipitation intensity. KF consistently captures both the initiation of this event and the intensification of precipitation after 06 UTC November 13th. Overall the eastward propagation of the system is also well captured. However, there is an overestimation of precipitation intensity during the first hours which is larger when KF is combined with the MYJ scheme. GF also performs well in this case, particularly capturing a second pulse of convective

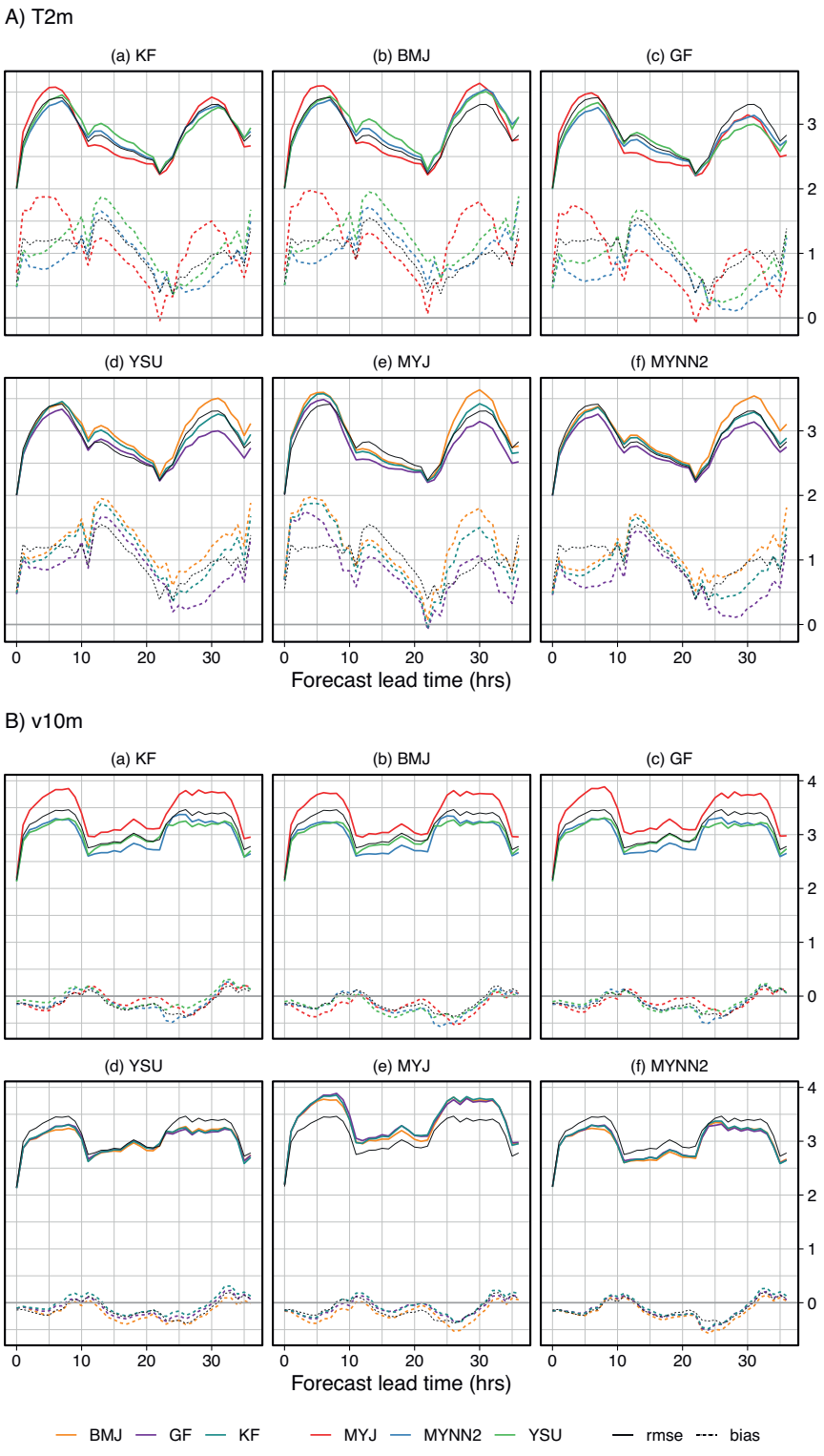

Fig. 15. Spatial and temporal averaged RMSE and BIAS with respect to CSWS and ASWS observations as a function of the forecast lead time, for RRR forecasts initialized at 12 UTC for (A) T2m [K] and (B) V10m [ms^{-1}]. Ensemble members with cumulus parameterizations of: (a) KF (b) BMJ and (c) GF; and with PBL parameterizations of: (d) YSU (e) MYJ and (f) MYNN2. For each case of cumulus (PBL) parameterizations the three possible combinations with PBL (cumulus) are shown. All the panels include the scores of the ensemble mean (grey thin contour).

initiation around 00 UTC November 13th which is not well represented by KF, although the maximum precipitation is split into two local maxima a few hours prior and after the observed one. Particularly, the prior maximum is significantly reduced by the GF-MYNN2 configuration.

An important issue is the clustering effect associated with the use of multi-physics ensembles. Fig. 17 shows different precipitation forecast clusters depending on the cumulus scheme, while the impact of PBL seems to play a secondary role for this variable. Also a look at the individual ensemble members reveals that differences among cumulus parameterizations are much larger than differences due to different initial conditions (not shown). This result confirms what has been found by Johnson et al. (2011), that in a multi-model multi-physics ensemble the spread at short lead times is dominated by the different physics schemes, at least for variables whose dynamics are directly driven by the parameterization of unresolved physical processes.

Overall, the performance of different schemes depend on the verified variable. For example, MYJ shows the largest RMSE for V10m for all

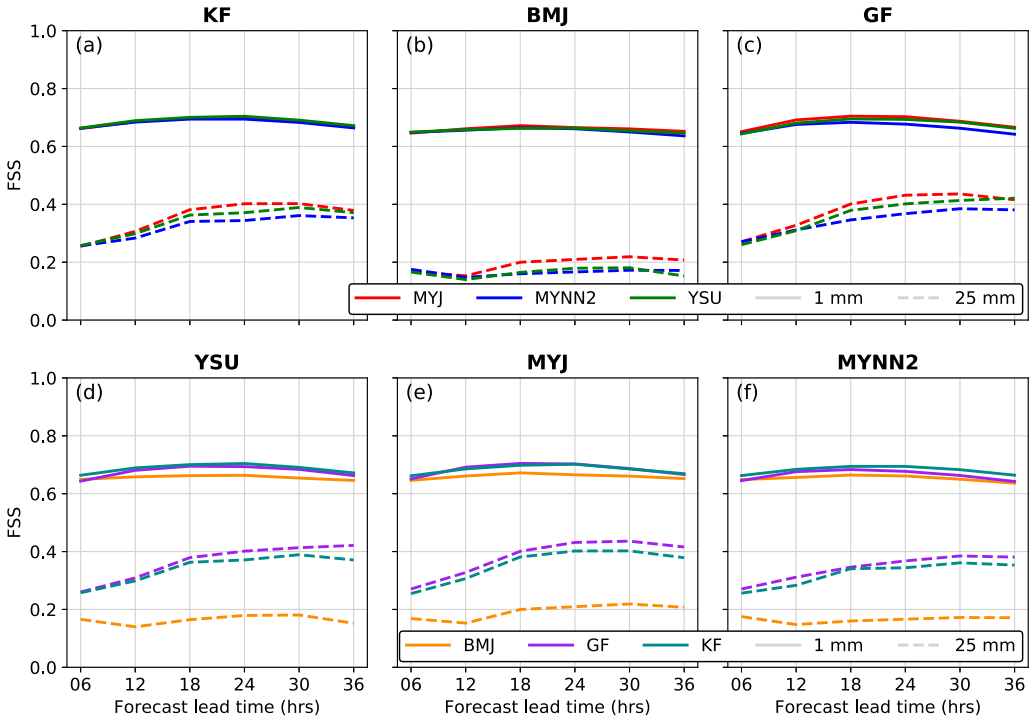

Fig. 16. As in Fig. 12, but for a box size of 50 km, and thresholds of 1 mm (solid line) and 25 mm (dashed line). Ensemble members with cumulus parameterizations of: (a) KF (b) BMJ and (c) GF; and with PBL parameterizations of: (d) YSU (e) MYJ and (f) MYNN2. For each case of cumulus (PBL) parameterizations the three possible combinations with PBL (cumulus) are shown.

forecast times and for T2m during daytime. At the same time, this parameterization produces the best results in terms of precipitation as revealed by the FSS. This confirms that no single model configuration overhangs and that all the evaluated combinations of schemes lead to similar forecast skill, with the exception of configurations using BMJ which showed lower forecast skill for almost all the variables considered. The fact that BMJ performs worse than the rest of the configurations suggests that this parameterization should not be included in the design of multi-physics ensembles over this region.

In addition, this indicates the need to account for the performance of individual schemes' combinations for forecasting and data assimilation. As an alternative to a-prior evaluation of different parameterizations combinations (that can be computationally demanding), some previous works explored on-line optimization schemes for multi-model ensemble compositions based on Bayesian techniques with promising results (e.g. Otsuka and Miyoshi (2015); Xue and Zhang (2014)).

5. Concluding remarks

This article documents the implementation of a regional ensemble data assimilation system during the RELAMPAGO field campaign in central Argentina, during November and December 2018. A multi-physics 60-member ensemble-based LETKF-WRF DA system was run in real-time to support IOP operations during the field campaign and also to provide the first set of analyses that can be used in research activities. This RELAMPAGO Rapid Refresh system (RRR) represents the first ensemble rapid update cycle that was run in Southern South America using conventional, satellite and radar observations altogether with a 10-km horizontal resolution.

On the one hand, the evaluation of the hourly analyses from 00 UTC 9 November to 12 UTC 19 December 2018 revealed an overall good performance when compared with the ERA5 reanalyses. Moreover, it was shown that the LETKF DA has functioned in a stable way during the whole period producing reasonable updates from the observations. Regarding the ensemble spread, the under dispersive estimation encountered is an aspect that should be addressed in future implementations, for example by optimizing the inflation coefficient, including perturbations on soil conditions, among others (Houtekamer and Zhang, 2016). The model uncertainties can also be handled by applying a stochastic kinetic energy backscatter scheme (Berner et al., 2011; Romine et al., 2014), with the aim of increasing the ensemble spread.

On the other hand, the assessment of 36 h forecasts initialized at different times presented an acceptable skill. It was shown that the WRF model produced warmer low level temperatures for almost all the hours of the day, in agreement with previous studies over the region (eg. Ruiz et al. (2010)). In relation to the vertical profiles of BIAS and RMSE with respect to Villa Yacanto radiosondes valid at 12 UTC, the misrepresentation of the humidity was the most striking feature, while the winds and temperature showed typical error values. With regards to precipitation, the Fractions Skill Scores were better for initializations at 00 and 12 UTC than at 06 and 18 UTC (considering IMERGFR).

In addition, these 36 h warm-start forecasts were compared with the cold-start forecasts of a 60-member WRF ensemble without LETKF application (named NoRegDA), showing an overall similar performance between them, but only a few times a positive impact of the regional warm-start initialization was encountered. Some possible reasons could be: (a) for RRR no radiance observations were assimilated (currently under development by the authors); (b) the low level temperature BIAS of WRF over the region, which has also been documented previously (Ruiz et al., 2010; Dillon et al., 2016) (other PBL schemes should be tested over the region and also a BIAS correction could be implemented (for example following Pelosi et al. (2017))); (c) the relatively low resolution of the regional model in comparison to the resolution in the global one, which prevents the regional model from producing better quality forecasts with respect to the driving global model; (d) the relatively small regional domain which may increase the negative effect associated with a coarse temporal resolution specification of the boundary conditions; (e) the dominant amount of radar observations compared to the other data sources which may produce a detrimental

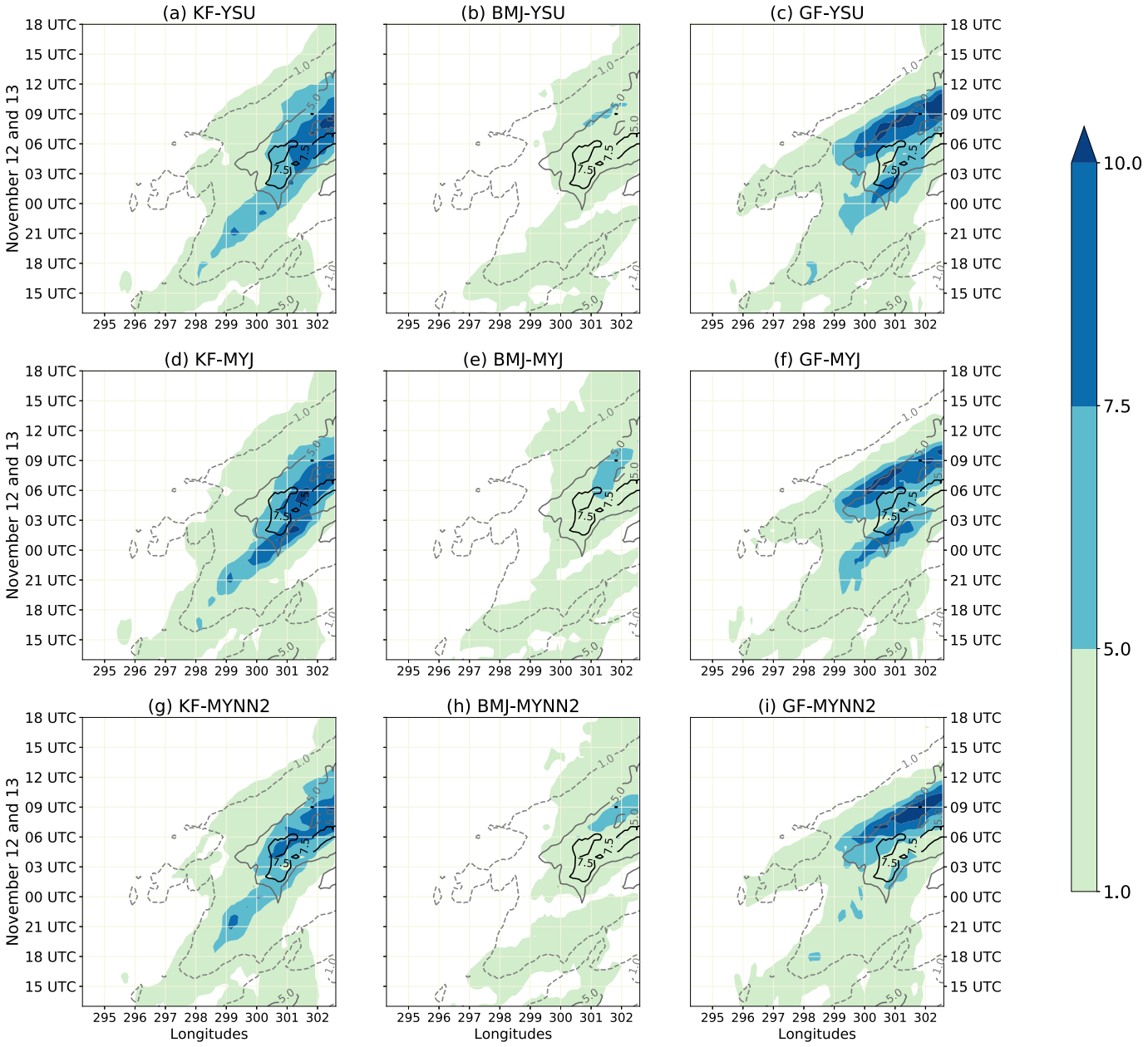

Fig. 17. Hourly precipitation Hovmöller diagrams for the 36 h forecasts initialized at 12 UTC on 12 November, for the RRR ensemble mean for each group of parameterizations (shaded) [mmh^{-1}]: (a)KF-YSU, (b)BMJ-YSU, (c)GF-YSU, (d)KF-MYJ, (e)BMJ-MYJ, (f)GF-MYJ, (g)KF-MYNN2, (h)BMJ-MYNN2, (i)GF-MYNN2. The IMERGFR contours for 1, 5 and 7.5 mmh^{-1} are also shown.

effect on the analysis, since radar data is complex to assimilate due to the nonlinear relation with model variables and also due to complex observational errors. It is evident that more work is required to improve the regional system to overcome current limitations and to provide a set of initial conditions for warm-start regional ensemble forecasts with better skill than the cold-start forecasts.

The analysis of the observation impact, using both ERA5 and Villa Yacanto soundings as reference data sets, showed that the assimilation usually lead to an error reduction in the forecast. However, a detrimental effect has been identified for some levels and variables like, for example, low-level temperature. This detrimental effect deserves further investigation. A detailed analysis of the impact associated with different observation types is currently underway.

In this work, we evaluated the individual skill of the nine model configurations used in the multi-physics ensemble. As has been reported in previous studies, no single combination of schemes produce the best results for all the verified variables (e.g. Ha et al. (2015)). The best combinations for forecasting surface variables (GF-MYNN2 and GF-YSU) differ from the best ones for forecasting precipitation (GF-MYJ and KF-MYJ). In addition, members using the BMJ cumulus parameterization performed systematically worse than those using GF or KF independently of the choice of the PBL scheme. Besides, the analysis of a particular case showed that using different schemes leads to different convective initiation times and different evolution of the precipitation systems.

Furthermore, a clustering effect similar to that reported in Johnson et al. (2011) has been found. As has been discussed in those papers, the clustering effect has important implications in the context of ensemble forecasting since the assumption of all members being equally likely is violated. This can have important consequences in the context of data

assimilation. Systematic differences among clusters of ensemble members may lead to systematic error covariances. Moreover the sample distribution derived from a multi-physics ensemble may depart from Guassianity, with eventually multiple modes associated to different clusters, thus violating the Kalman filter assumptions and leading to sub-optimal analysis updates. These effects deserves further investigation, particularly for the assimilation of radar data and surface observations which are linked to model variables that are susceptible of being affected by these issues.

We foster the usage of the RRR data set to study the RELAMPAGO IOPs in order to analyze both the strengths and weaknesses of the DA system, which could be taken into account in future experimental designs either for research or operational implementations over the region. For example, some aspects that should be addressed concerning an improvement in the DA system are: the quality control of the observations to be assimilated, particularly the ones from radar and surface stations; the superobbing applied for dense distributed observations (for example considering the radar data altogether for the calculation); the temporal frequency used for the assimilation of radar data; the values given for certain LETKF parameters, as the localization and the inflation; among others. Sensitivity experiments to study these improvements can be validated with RELAMPAGO's observations.

Last but not least, a project to evaluate the impact of the assimilation of the observations collected during the campaign is underway. Besides, the findings documented in this article have been taken into account for the design of a convection-permitting regional LETKF-WRF system, to be implemented at the ANMS.

Declaration of Competing Interest

There are no interests to declare for any of the authors of the manuscript "A Rapid Refresh ensemble based Data Assimilation and Forecast system for the RELAMPAGO field campaign", submitted in December 2020.

Acknowledgements

We are very thankful to the Argentinian National Meteorological Service (ANMS), the National Scientific and Technical Research Council (CONICET), the University of Buenos Aires (UBA) and the Atmospheric and Sea Research Center (CIMA), who support this project. We acknowledge the Cheyenne HPC resources (doi:https://doi.org/10.5065/D6RX99HX) from NCAR's Computational and Information Systems Laboratory, National Science Foundation (project code UIUC0012). Also, PIDDEF 16/2014, PICT 2014–1000, PICT 2017–0221 and PICT 2018–3202 grants partially funded this project. SWN acknowledges support from National Science Foundation grant AGS-1661799. For the LETKF-WRF a modified version of the code available at https://github.com/takemasa-miyoshi/letkf was used, including the radar observations operator. For post processing issues NCL, Python and R packages were used. Finally, we acknowledge Dr. Victoria Galligani for her suggestions and the anonymous reviewers for their enrichment comments.

Appendix A

Table A1 lists the Automatic Surface Weather Stations (ASWS) providers along with their web sites. The data was collected during the RELAMPAGO field campaign.

Table A1
Automatic surface weather stations providers and their web sites.

ASWS Provider	web site
REM San Luis	http://www.clima.edu.ar/
Entre Ríos Board of Trade	http://www.centrales.bolsacer.org.ar/
Córdoba Board of Trade	http://clima.bccba.com.ar/
Chaco Provincial Government	http://clima.produccion.chaco.gov.ar/
Córdoba Provincial Government	http://magya.omixom.com/
National Water Institute (INA)	http://sgainacirsa.ddns.net/
National Institute for Agricultural Technology (INTA)	http://inta.gob.ar/
Entre Ríos Provincial Government	http://www.hidraulica.gob.ar/
Rosario Board of Trade	http://www.bcr.com.ar/
Wunderground	http://wunderground.com/
La Plata National University	http://unlp.edu.ar/
Uruguay National Weather Service	http://inumet.gub.uy/
Brasil National Weather Service	http://www.inmet.gov.br/
La Pampa Provincial Government	http://www.lapampa.gov.ar/
Tucumán Agroindustrial Experimental Station	http://www.eeaoc.org.ar/
Paraguay National Aeronautical Direction	http://www.dinac.gov.py/
Mendoza Radar Operators	http://mate.cima.fcen.uba.ar/estaciones/mendoza/

References

Aksoy, A., Dowell, D.C., Snyder, Chris, 2009. A multicase comparative assessment of the Ensemble Kalman Filter for assimilation of radar observations. Part I: Storm-scale analyses. Mon. Weather Rev. 137, 1805–1824. https://doi.org/10.1175/2008MWR2691.1.

Arruti, A., Maldonado, P., Rugna, M., Sacco, M., Ruiz, J.J., Vidal, L., 2021. Sistema de control de calidad de datos de radar en el Servicio Meteorológico Nacional - Parte I: Descripción del algoritmo. Nota Técnica SMN 86, 1–26. http://hdl.handle.net/20.500.12160/1537.

Barker, D., Huang, X.Y., Liu, Z., Auligné, T., Zhang, X., Rugg, S., Ajjaji, R., Bourgeois, A., Bray, J., Chen, Y., Demirtas, M., Guo, Y.R., Henderson, T., Huang, W., Lin, H.C., Michalakes, J., Rizvi, S., Zhang, X., 2012. The weather research and forecasting model's community variational/ensemble data assimilation system: WRFDA. Bull. Am. Meteorol. Soc. 93, 831–843. https://doi.org/10.1175/BAMS-D-11-00167.1.

Bauce Machado, V., Gustavo de Goncalves, L., Vendrasco, E., Sinhori, N., Herdies, D., Sapucci, L., Levien, C., Quadro, M., Rodrigues, T., Cardoso, C., Biscaro, T., 2017. Investigating the impacts of convective scale hazardous weather events in Santa Catarina State through the CPTEC/INPE local data assimilation system. In: Seventh International WMO Symposium on Data Assimilation.

Benjamin, S.G., Weygandt, S.S., Brown, J.M., Hu, M., Alexander, C.R., Smirnova, T.G., Olson, J.B., James, E.P., Dowell, D.C., Grell, G.A., Lin, H., Peckham, S.E., Smith, T.L., Moninger, W.R., Kenyon, J.S., Manikin, G.S., 2016. A north american hourly assimilation and model forecast cycle: the rapid refresh. Mon. Weather Rev. 144, 1669–1694. https://doi.org/10.1175/MWR-D-15-0242.1.

Berner, J., Ha, S.Y., Hacker, J.P., Fournier, A., Snyder, C., 2011. Model uncertainty in a Mesoscale Ensemble Prediction System: Stochastic versus Multiphysics Representations. Mon. Weather Rev. 139, 1972–1995. https://doi.org/10.1175/2010MWR3595.1.

Carrió, D., Homar, V., Wheatley, D., 2019. Potential of an EnKF storm-scale data assimilation system over sparse observation regions with complex orography. Atmos. Res. 216, 186–206. https://doi.org/10.1016/j.atmosres.2018.10.004.

Casaretto, G., Dillon, M.E., Salio, P., García Skabar, Y., Nesbitt, S., Schumacher, R., García, C.M., Catalini, C., 2021. High-resolution NWP forecast precipitation comparison over complex terrain of the sierras de Córdoba during RELAMPAGO-CACTI. Weather Forecast. Submitted for publication.

Computational and Information Systems Laboratory, 2019. Cheyenne: HPE/SGI ICE XA System (University Community Computing). National Center for Atmospheric Research Boulder, CO. https://doi.org/10.5065/D6RX99HX.

Corrales, P., Ruiz, J.J., Galligani, V., Sacco, M., Dillon, M.E., García Skabar, Y., Sapucci, L., Nesbitt, S., 2019. Assimilation of conventional observations in a deep convection case during RELAMPAGO using the WRF-GSI-LETFK system. In: RELAMPAGO-CACTI Data Analysis Workshop, Buenos Aires, Argentina.

Dillon, M.E., García Skabar, Y., Ruiz, J., Kalnay, E., Collini, E.A., Echevarría, P., Saucedo, M., Miyoshi, T., Kunii, M., 2016. Application of the WRF-LETKF Data Assimilation System over Southern South America: sensitivity to Model Physics. Weather Forecast. 31, 217–236. https://doi.org/10.1175/WAF-D-14-00157.1.

Dillon, M.E., García Skabar, Y., Kalnay, E., Ruiz, J.J., Collini, E.A., 2019. Sensibilidad de un sistema de asimilación de datos por ensambles a diferentes configuraciones, implementado en el sur de Sudamérica. Meteorológica 44, 15–34.

de Elía, R., Vidal, L., Lohigorry, P., Mezher, R., Rugna, M., 2017. El SMN y la red argentina de radares meteorológicos de Argentina. Nota Técnica SMN 39, 1–21. http://hdl.handle.net/20.500.12160/625.

Ferreira, R.C., Herdies, D.L., Vendrasco, É.P., Beneti, C.A.A., Biscaro, T.S., 2017. Impacto da Assimilação de Dados de Radar em Sistemas Convectivos de Mesoescala: Um Estudo de Caso. Rev. Brasil. Meteorol. 32, 447–458. https://doi.org/10.1590/0102-77863230011.

Ferreira, R.C., Alves Júnior, M.P., Vendrasco, É.P., Aravéquia, J.A., Nolasco Junior, L.R., Biscaro, T.S., Ferreira, R.C., Alves Júnior, M.P., Vendrasco, É.P., Aravéquia, J.A., Nolasco Junior, L.R., Biscaro, T.S., 2020. Impacto das Parametrizações de Microfísica na Previsão de Precipitação utilizando Assimilação de Dados de Radar. Rev. Brasil. Meteorol. 35, 123–134. https://doi.org/10.1590/0102-7786351005.

Fortin, V., Abaza, M., Anctil, F., Turcotte, R., 2014. Why should Ensemble Spread Match the RMSE of the Ensemble mean? J. Hydrometeorol. 15, 1708–1713. https://doi.org/10.1175/JHM-D-14-0008.1.

Gao, S., Min, J., Liu, L., Ren, C., 2019. The development of a hybrid EnSRF-En3DVar system for convective-scale data assimilation. Atmos. Res. 229, 208–223. https://doi.org/10.1016/j.atmosres.2019.06.024.

García Skabar, Y., Matsudo, C., Hobouchian, M.P., Ruiz, J., Righetti, S., 2018. Implementación del modelo WRF en alta resolución en el Servicio Meteorológico Nacional. In: CAM (Ed.), XIII CONGREMET, Rosario, Santa Fe, Argentina. CAM.

Geer, A.J., Lonitz, K., Weston, P., Kazumori, M., Okamoto, K., Zhu, Y., Liu, E.H., Collard, A., Bell, W., Migliorini, S., Chambon, P., Fourrié, N., Kim, M.J., Köpken-Watts, C., Schraff, C., 2018. All-sky satellite data assimilation at operational weather forecasting centres. Q. J. R. Meteorol. Soc. 144, 1191–1217. https://doi.org/10.1002/qj.3202.

Goncalves de Goncalves, L.G., Sapucci, L., Vendrasco, E., de Mattos, J.G., Ferreira, C., Khamis, E., Cruz, N., 2015. A Rapid Update Data Assimilation Cycle Over South America using 3DVar and EnKF.

Grell, G.A., Freitas, S.R., 2013. A scale and aerosol aware stochastic convective parameterization for weather and air quality modeling. Atmos. Chem. Phys. Discus. 13, 23845–23893. https://doi.org/10.5194/acpd-13-23845-2013.

Greybush, S.J., Kalnay, E., Miyoshi, T., Ide, K., Hunt, B.R., 2011. Balance and Ensemble Kalman Filter Localization Techniques. Mon. Weather Rev. 139, 511–522. https://doi.org/10.1175/2010MWR3328.1.

Gustafsson, N., Janjić, T., Schraff, C., Leuenberger, D., Weissmann, M., Reich, H., Brousseau, P., Montmerle, T., Wattrelot, E., Bučánek, A., Mile, M., Hamdi, R., Lindskog, M., Barkmeijer, J., Dahlbom, M., Macpherson, B., Ballard, S., Inverarity, G., Carley, J., Alexander, C., Dowell, D., Liu, S., Ikuta, Y., Fujita, T., 2018. Survey of data assimilation methods for convective-scale numerical weather prediction at operational centres. Q. J. R. Meteorol. Soc. 144, 1218–1256. Doi:https://doi.org/10.1002/qj.3179 .

Ha, S., Berner, J., Snyder, C., 2015. A comparison of model error representations in mesoscale ensemble data assimilation. Mon. Weather Rev. 143, 3893–3911. https://doi.org/10.1175/MWR-D-14-00395.1.

Hersbach, H., Dee, D., 2016. ERA5 Reanalysis Is in Production. Technical Report. ECMWF Newsletter, Vol. 147.

Hong, S.Y., Kim, J.H., Lim, J.o., Dudhia, J., 2006a. The WRF single moment 6-Class Microphysics Scheme (WSM6). J. Korean Meteorol. Soc. 42, 129–151.

Hong, S.Y., Noh, Y., Dudhia, J., 2006b. A New Vertical Diffusion Package with an Explicit Treatment of Entrainment Processes. Mon. Weather Rev. 134, 2318–2341. https://doi.org/10.1175/MWR3199.1.

Houtekamer, P.L., Zhang, F., 2016. Review of the ensemble Kalman filter for atmospheric data assimilation. Mon. Weather Rev. 144, 4481–4532. https://doi.org/10.1175/MWR-D-15-0440.1.

Huffman, G., Bolvin, D., Braithwaite, D., Hsu, K., Joyce, R., Kidd, C., Nelkin, E., Sorooshian, S., Tan, J., Xie, P., 2018. NASA Global Precipitation Measurement (GPM) Integrated Multi-satellitE Retrievals for GPM (IMERG). Technical Report. National Aeronautics and Space Administration (NASA).

Hunt, B.R., Kostelich, E.J., Szunyogh, I., 2007. Efficient data assimilation for spatiotemporal chaos: a local ensemble transform Kalman filter. Phys. D: Nonlinear Phenom. 230, 112–126. https://doi.org/10.1016/j.physd.2006.11.008.

Iacono, M.J., Delamere, J.S., Mlawer, E.J., Shephard, M.W., Clough, S.A., Collins, W.D., 2008. Radiative forcing by long-lived greenhouse gases: calculations with the AER radiative transfer models. J. Geophys. Res. 113, D13103 https://doi.org/10.1029/2008JD009944.

Janjić, Z.I., 1994. The Step-Mountain Eta coordinate model: further developments of the convection, viscous sublayer, and turbulence closure schemes. Mon. Weather Rev. 122, 927–945. https://doi.org/10.1175/1520-0493(1994)122<0927:TSMECM>2.0.CO;2.

Johnson, A., Wang, X., Xue, M., Kong, F., 2011. Hierarchical cluster analysis of a convection-allowing ensemble during the hazardous weather testbed 2009 spring experiment. Part ii: ensemble clustering over the whole experiment period. Mon. Weather Rev. 139, 3694–3710. https://doi.org/10.1175/MWR-D-11-00016.1.

Jones, T.A., Stensrud, D., Wicker, L., Minnis, P., Palikonda, R., 2015. Simultaneous radar and satellite data storm-scale assimilation using an ensemble kalman filter approach for 24 May 2011. Mon. Weather Rev. 143, 165–194. https://doi.org/10.1175/MWR-D-14-00180.1.

Kain, J.S., 2004. The Kain–Fritsch Convective Parameterization: an Update. J. Appl. Meteorol. 43, 12.

Koizumi, K., Ishikawa, Y., Tsuyuki, T., 2005. Assimilation of Precipitation Data to the JMA Mesoscale Model with a Four-dimensional Variational Method and its Impact on Precipitation forecasts. SOLA 1, 45–48. https://doi.org/10.2151/sola.2005-013.

Kunii, M., 2014. Mesoscale data assimilation for a local severe rainfall event with the NHM–LETKF system. Weather Forecast. 29, 1093–1105. https://doi.org/10.1175/WAF-D-13-00032.1.

Kuroda, T., Fujita, T., Seko, H., Saito, K., 2012. Construction of Mesoscale LETKF Data Assimilation Experiment System, p. 3.

Lange, H., Craig, G.C., 2014. The impact of data assimilation length scales on analysis and prediction of convective storms. Mon. Weather Rev. 142, 3781–3808. https://doi.org/10.1175/MWR-D-13-00304.1.

Lien, G.Y., Miyoshi, T., Nishizawa, S., Yoshida, R., Yashiro, H., Adachi, S.A., Yamaura, T., Tomita, H., 2017. The Near-Real-Time SCALE-LETKF System: A Case of the September 2015 Kanto-Tohoku Heavy Rainfall. SOLA 13, 1–6. https://doi.org/10.2151/sola.2017-001.

Maldonado, P., Ruiz, J.J., Saulo, C., Honda, T., Miyoshi, T., 2019. Assimilation of radar observations using the SCALE-LETKF: A case study during RELAMPAGO. In: RELAMPAGO-CACTI Data Analysis Workshop, Buenos Aires, Argentina.

Maldonado, P., Ruiz, J., Saulo, C., 2021. Sensitivity to initial and boundary perturbations in convective-scale ensemble-based data assimilation: Imperfect-model osses. SOLA 17, 96–102. https://doi.org/10.2151/sola.2021-015.

Matsudo, C., Salles, M.A., García Skabar, Y., 2021. Verificación de los pronósticos del esquema determinístico del modelo WRF para el año 2020. Nota Técnica SMN 95, 1–28. http://hdl.handle.net/20.500.12160/1595.

Miyoshi, T., Aranami, K., 2006. Applying a Four-dimensional Local Ensemble Transform Kalman Filter (4D-LETKF) to the JMA Nonhydrostatic Model (NHM). SOLA 2, 128–131. https://doi.org/10.2151/sola.2006-033.

Miyoshi, T., Kunii, M., 2012a. The Local Ensemble Transform Kalman Filter with the Weather Research and forecasting Model: experiments with Real Observations. Pure Appl. Geophys. 169, 321–333. https://doi.org/10.1007/s00024-011-0373-4.

Miyoshi, T., Kunii, M., 2012b. Using AIRS retrievals in the WRF-LETKF system to improve regional numerical weather prediction. Tellus A: Dyn. Meteorol. Oceanogr. 64, 18408. https://doi.org/10.3402/tellusa.v64i0.18408.

Nakanishi, M., Niino, H., 2009. Development of an improved Turbulence Closure Model for the Atmospheric Boundary Layer. J. Meteorol. Soc. Jpn. 87, 895–912. https://doi.org/10.2151/jmsj.87.895.

Necker, T., Geiss, S., Weissmann, M., Ruiz, J., Miyoshi, T., Lien, G.Y., 2020. A convective-scale 1,000-member ensemble simulation and potential applications. Q. J. R. Meteorol. Soc. 146, 1423–1442. https://doi.org/10.1002/qj.3744.

Nesbitt, S.W., Salio, P.V., Ávila, E., Bitzer, P., Carey, L., Chandrasekar, V., Deierling, W., Dominguez, F., Dillon, M.E., Garcia, C.M., Gochis, D., Goodman, S., Hence, D.A., Kosiba, K.A., Kumjian, M.R., Lang, T., Marquis, J., Marshall, R., McMurdie, L.A., Nascimento, E.L., Rasmussen, K.L., Roberts, R., Rowe, A.K., Ruiz, J.J., São Sabbas, E. F., Saulo, A.C., Schumacher, R.S., Garcia Skabar, Y., Toledo Machado, L.A., Trapp, R. J., Varble, A., Wilson, J., Wurman, J., Zipser, E.J., Arias, I., Bechis, H., Grover, M.A., 2021. A storm safari in subtropical south america: proyecto RELAMPAGO. Bull. Am. Meteorol. Soc. 1–63. https://doi.org/10.1175/BAMS-D-20-0029.1.

Niu, G.Y., Yang, Z.L., Mitchell, K.E., Chen, F., Ek, M.B., Barlage, M., Kumar, A., Manning, K., Niyogi, D., Rosero, E., Tewari, M., Xia, Y., 2011. The community Noah land surface model with multiparameterization options (Noah-MP): 1. Model description and evaluation with local-scale measurements. J. Geophys. Res. 116, D12109 https://doi.org/10.1029/2010JD015139.

Otsuka, S., Miyoshi, T., 2015. A bayesian optimization approach to multimodel ensemble kalman filter with a low-order model. Mon. Weather Rev. 143, 2001–2012. https://doi.org/10.1175/MWR-D-14-00148.1.

Pal, S., Dominguez, F., Dillon, M.E., Alvarez, J., Garcia, C.M., Nesbitt, S.W., Gochis, D., 2021. Hydrometeorological observations and modeling of an extreme rainfall event using WRF and WRF-Hydro during the RELAMPAGO field campaign in Argentina. J. Hydrometeorol. 22, 331–351. https://doi.org/10.1175/JHM-D-20-0133.1.

Pan, Y., Xue, M., Zhu, K., Wang, M., 2018. A prototype regional GSI-based EnKF-Variational hybrid data assimilation system for the rapid refresh forecasting system: Dual-resolution implementation and testing results. Adv. Atmos. Sci. 35, 518–530. https://doi.org/10.1007/s00376-017-7108-0.

Pelosi, A., Medina, H., Van den Bergh, J., Vannitsem, S., Chirico, G.B., 2017. Adaptive Kalman Filtering for Postprocessing Ensemble Numerical Weather predictions. Mon. Weather Rev. 145, 4837–4854. https://doi.org/10.1175/MWR-D-17-0084.1.

Piersante, J.O., Schumacher, R.S., Rasmussen, K.L., 2021. Comparison of biases in warm-season wrf forecasts in north and south america. Weather Forecast. 36, 979–10001. https://doi.org/10.1175/WAF-D-20-0062.1.

Putnam, B.J., Xue, M., Jung, Y., Snook, N.A., Zhang, G., 2017. Ensemble probabilistic prediction of a mesoscale convective system and associated polarimetric radar variables using single-moment and double-moment microphysics schemes and EnKF radar data assimilation. Mon. Weather Rev. 145, 2257–2279. https://doi.org/10.1175/MWR-D-16-0162.1.

Roberts, N., 2008. Assessing the spatial and temporal variation in the skill of precipitation forecasts from an NWP model. Meteorol. Appl. 15, 163–169. https://doi.org/10.1002/met.57.

Romine, G.S., Schwartz, C.S., Berner, J., Fossell, K.R., Snyder, C., Anderson, J.L., Weisman, M.L., 2014. Representing forecast error in a convection-permitting ensemble system. Mon. Weather Rev. 142, 4519–4541. https://doi.org/10.1175/MWR-D-14-00100.1.

Routray, A., Mohanty, U.C., Rizvi, S.R.H., Niyogi, D., Osuri, K.K., Pradhan, D., 2010. Impact of Doppler weather radar data on numerical forecast of Indian monsoon depressions. Q. J. R. Meteorol. Soc. 136, 1836–1850. https://doi.org/10.1002/qj.678.

Ruiz, J.J., Saulo, C., Nogués-Paegle, J., 2010. WRF model sensitivity to choice of parameterization over South America: validation against surface variables. Mon. Weather Rev. 138, 3342–3355. https://doi.org/10.1175/2010MWR3358.1.

Schumacher, R.S., Hence, D.A., Nesbitt, S.W., Trapp, R.J., Kosiba, K.A., Wurman, J., Salio, P., Rugna, M., Varble, A.C., Kelly, N.R., 2021. Convective-storm environments in subtropical south america from high-frequency soundings during RELAMPAGO-CACTI. Mon. Weather Rev. 149, 1439–1458. https://doi.org/10.1175/MWR-D-20-0293.1.

Skamarock, W., Klemp, J., Dudhi, J., Gill, D., Barker, D., Duda, M., Huang, X.Y., Wang, W., Powers, J., 2008. A Description of the Advanced Research WRF Version 3. Technical Report NCAR/TN-475+STR. NCAR.

Susskind, J., Blaisdell, J.M., Iredell, L., 2014. Improved methodology for surface and atmospheric soundings, error estimates, and quality control procedures: the atmospheric infrared sounder science team version-6 retrieval algorithm. J. Appl. Remote. Sens. 8, 084994 https://doi.org/10.1117/1.JRS.8.084994.

Tobin, D.C., Revercomb, H.E., Knuteson, R.O., Lesht, B.M., Strow, L.L., Hannon, S.E., Feltz, W.F., Moy, L.A., Fetzer, E.J., Cress, T.S., 2006. Atmospheric Radiation Measurement site atmospheric state best estimates for Atmospheric Infrared Sounder temperature and water vapor retrieval validation. J. Geophys. Res. 111, D09S14 https://doi.org/10.1029/2005JD006103.

Tong, M., Xue, M., 2005. Ensemble Kalman Filter Assimilation of Doppler Radar Data with a Compressible Nonhydrostatic Model: OSS experiments. Mon. Weather Rev. 133, 1789–1807. https://doi.org/10.1175/MWR2898.1.

Toshio Inouye, R., Calvetti, L., Gonçalves, J., Maske, B., Neundorf, R., Beneti, C., Diniz, F., Vendrasco, E., Herdies, D., Gustavo de Goncalves, L., 2017. Impact of radar data assimilation on a severe storm study in brazil. In: 97th American Meteorological Meeting Annual Meeting, Seattle, WA.

UCAR/NCAR, Earth Observing Laboratory, 2020. Multi-network Composite Highest Resolution Radiosonde Data. Version 1.3. UCAR/NCAR - Earth Observing Laboratory. https://doi.org/10.26023/GKFF-YNBJ-BV14.

Vendrasco, E.P., Machado, L.A.T., Araujo, C.S., Ribaud, J.F., Ferreira, R.C., 2020. Potential use of the GLM for nowcasting and data assimilation. Atmos. Res. 242, 105019. https://doi.org/10.1016/j.atmosres.2020.105019.

Vera, C., Baez, J., Douglas, M., Emmanuel, C.B., Marengo, J., Meitin, J., Nicolini, M., Nogues-Paegle, J., Paegle, J., Penalba, O., Salio, P., Saulo, C., Silva Dias, M.A., Dias, P.S., Zipser, E., 2006. The south american low-level jet experiment. Bull. Am. Meteorol. Soc. 87, 63–78. https://doi.org/10.1175/BAMS-87-1-63.

Whitaker, J.S., Hamill, T.M., 2012. Evaluating Methods to Account for System Errors in Ensemble Data Assimilation. Mon. Weather Rev. 140, 3078–3089. https://doi.org/10.1175/MWR-D-11-00276.1.

Xiao, Q., Kuo, Y.H., Sun, J., Lee, W.C., Lim, E., Guo, Y.R., Barker, D.M., 2005. Assimilation of Doppler Radar Observations with a Regional 3DVAR System: Impact of Doppler Velocities on forecasts of a Heavy Rainfall Case. J. Appl. Meteorol. 44, 768–788. https://doi.org/10.1175/JAM2248.1.

Xue, L., Zhang, D., 2014. A multimodel data assimilation framework via the ensemble kalman filter. Water Resour. Res. 50, 4197–4219. https://doi.org/10.1002/2013WR014525.

Zhou, X., Zhu, Y., Hou, D., Luo, Y., Peng, J., Wobus, R., 2017. Performance of the New NCEP Global Ensemble Forecast System in a parallel Experiment. Weather Forecast. 32, 1989–2004. https://doi.org/10.1175/WAF-D-17-0023.1.

Zhu, K., Xue, M., Pan, Y., Hu, M., Benjamin, S.G., Weygandt, S.S., Lin, H., 2019. The Impact of Satellite Radiance Data Assimilation within a frequently Updated Regional Forecast System using a GSI-based Ensemble Kalman Filter. Adv. Atmos. Sci. 36, 1308–1326. https://doi.org/10.1007/s00376-019-9011-3.